Title
Quantitative Imaging in Cell Biology

Author
Yassif, Jaime

Publication Date
2012

Peer reviewed|Thesis/dissertation

Quantitative Imaging in Cell Biology

by

Jaime Mirit Yassif

A dissertation submitted in partial satisfaction of the
requirements for the degree of
Doctor of Philosophy

in

Biophysics

in the

Graduate Division

of the

University of California, Berkeley

Committee in charge:
Professor Jan T. Liphardt, Chair
Professor Daniel Fletcher
Professor Eva Nogales
Professor Karsten Weis

Fall 2012

Abstract

Quantitative Imaging in Cell Biology

by

Jaime Mirit Yassif

Doctor of Philosophy in Biophysics

University of California, Berkeley

Professor Jan T. Liphardt, Chair

Cells perform a range of complex functions to maintain homeostasis, including regulation of gene expression, selective trafficking of molecules between subcellular compartments, and protein expression. These processes are mediated by dynamic complexes of proteins and other molecules. Quantitative imaging in biology is concerned with answering questions about the spatial distribution, dynamics and conformational changes of these complexes as they perform their biological functions. This study utilizes a range of quantitative imaging techniques—including plasmon rulers, quantitative fluorescence microscopy, fluorescence recovery after photobleaching (FRAP), and super-resolution imaging—to answer biologically relevant questions.

Microorganisms often contend with fluctuating environmental conditions and shifting metabolic demands, and their survival depends on their ability to rapidly alter gene expression. In bacteria, rapid regulation of gene expression is facilitated by transcription attenuation and anti-termination mechanisms that involve the binding of proteins to RNA and the manipulation of RNA structure. In *Bacillus* species the trp RNA-binding Attenuation Protein (TRAP) modulates the expression of the tryptophan biosynthetic pathway by binding messenger RNA and interfering with transcription elongation. Chapter 2 describes work to characterize the mechanism of TRAP binding to RNA, utilizing a single-molecule method that employs RNA-linked pairs of gold nano-particles—plasmon rulers.

Eukaryotic cells segregate their genetic material into an envelope-bound nucleus, and all transport and communication between this compartment and the cytoplasm is mediated by the nuclear pore complex (NPC), a large multi-protein channel. NPC-mediated transport of materials between the cytoplasm and the nucleus is essential for many basic cell functions. The components of this molecular machine have been

characterized, and there are several unproven models that describe how these components might function in concert. However, the mechanism by which this system of molecules mediates selective, direction transport has yet to be elucidated.

The nuclear transport receptor importin-β, as well as Ran and Nup153 have been shown to be necessary for modulating selectivity of active and passive transport through the NPC. This study provides mechanistic details about importin-β interactions with the pore, which mediate selective, directional transport. Quantitative fluorescence microscopy, FRAP and super-resolution imaging are used to study the interplay of importin-β, Ran and Nup153 in regulating the selectivity and efficiency of the mammalian NPC. Chapter 3 describes the use of FRAP and inverse FRAP (iFRAP) to quantify the dynamics of importin-β turnover in the nuclear pore complex. Chapter 4 describes the use of super-resolution microscopy to characterize the distribution of importin-β in the NPC under a range of conditions.

This study characterizes the thermodynamics and kinetics of importin-β interaction with the NPC and shows how Ran and Nup153 mediate these interactions. Importin-β is an integral part of the NPC gate, and Ran acts to remodel this gate. The nucleoporin Nup153 plays a critical in the mechanism, acting as a coordinating site for importin-β and Ran action.

Thesis, Antithesis, Synthesis.

Contents

Acknowledgements

I would like to first thank my advisor Jan Liphardt for his support, guidance, and willingness to give me the space to try a wide range of experiments. I would also like to thank Karsten Weis for sharing his expertise on the nuclear pore complex and working with us to help guide this project. Members of my Thesis Committee, Eva Nogales and Dan Fletcher, as well as Jan and Karsten, have provided helpful feedback on this project and have been very flexible and generous with their time to help me complete my dissertation.

It has been a real pleasure working with Jeffrey Tang and Alan Lowe, as part of what has become known as 'Team NPC.' Jeff and Alan have made excellent collaborators, and it has been very rewarding to work with them and watch our story about the NPC come together. Throughout this process they have been fun partners in crime, and I have learned a great deal from them. I would like to extend special thanks to Alan Lowe for helping me learn how to code and do image processing. This project has been an empowering process that has helped me accomplish what I set out to do when I came to graduate school—quantitatively study biological systems and gain nerdy coding skills in the process—and I am grateful for that.

I would also like to thank all the members of the Liphardt Lab for providing a collaborative and entertaining environment throughout my time in graduate school. Special thanks go to Phil Jess for building many of the microscopes that keep our lab running, and for never ceasing to amaze with his fiercely fashionable wardrobe. Will Draper and Adam Politzer have made our lab a more lively place through technically elaborate pranks that have kept things interesting. Hanna Engleke has been an ongoing source of good cheer and amazing homemade cakes. Ann McEvoy has provided encouragement along the way, as well as a steady stream of questionable sweets from abroad with unknown expiry dates. Jess Walters, who supervised my rotation in the lab, continues to be a rockstar—literally and figuratively.

I would like to thank Kate Chase, our fearless and talented Biophysics Program Coordinator, for helping me keep on track during graduate school and for always being willing to offer support and a listening ear. It has been a pleasure to be a member of the Biophysics Graduate Group, which has provided a sense of community within our large university. Interactions with students and faculty in the

group have served a an ongoing source of support and motivation throughout my time in graduate school.

Finally, I would like to thank my community of friends—Nori, Ann, Alan, Mike, Matt, James, Emily, Carrie, Dave, Tali, Sam, Anna, Laura, John, Loring, Gil, and many more than I can name here. Your continued friendship has helped me keep perspective when times were tough, and my successes have become much more meaningful by celebrating them with you. I value the community that we have built together, and it continues to serve as a source of strength and joy.

Chapter 1
Introduction

1.1 - Overview

Cells perform a range of complex functions to maintain homeostasis, including regulation of gene expression, selective trafficking of molecules between subcellular compartments, and protein expression. In the past 15 years advances in microscopy have built the foundation for using imaging to characterize the molecular mechanisms of these processes, which involve dynamic complexes of multiple proteins. Ongoing improvements in temporal and spatial resolution in imaging have made it possible not only to qualitatively characterize the molecular mechanisms that underlie cell function but to extract quantitative information as well—making it possible to characterize the biophysics of these processes.

Quantitative imaging in biology is concerned with answering three types of questions about molecular behavior: How are molecules spatially distributed? What are the dynamics of their behavior? And what conformational changes do they undergo in performing their function? This study utilizes a range of quantitative imaging techniques and shows how they can be applied to answer biologically relevant questions.

Microorganisms often contend with fluctuating environmental conditions and shifting metabolic demands. Their survival depends on their ability to rapidly alter gene expression in a measured way to support continued function under new conditions. Gene expression is typically controlled through regulation of gene transcription initiation—by repressors and promoters that bind DNA. However,

once transcription has begun, the nascent RNA transcript is also a target for regulation. Bacteria use a variety of transcription attenuation and anti-termination mechanisms to regulate transcription elongation. These mechanisms involve the binding of proteins to RNA and the manipulation of its structure to fine tune gene expression, and they are commonly used in by enteric bacteria to regulate expression of genes involved in amino acid biosynthetic pathways. In *Bacillus* species the trp RNA-binding Attenuation Protein (TRAP) modulates the expression of the tryptophan biosynthetic pathway by binding messenger RNA and interfering with transcription elongation. The structural changes imposed by TRAP on its target RNA have been characterized as have the bulk binding kinetics. However, the mechanistic details of this process have yet to be elucidated. Chapter 2 describes work to characterize the mechanism of TRAP binding to RNA utilizing a single-molecule method that employs RNA-linked pairs of gold nano-particles—plasmon rulers.

Eukaryotic cells segregate their genetic material into an envelope-bound nucleus, and all transport and communication between this compartment and the cytoplasm is mediated by the nuclear pore complex (NPC), a large multi-protein channel. NPC-mediated transport of materials between the cytoplasm and the nucleus is essential for many basic cell functions. The NPC selectively imports proteins that are required for DNA maintenance and regulation of gene expression, and it exports messenger RNA-nucleoprotein complexes to the cytoplasm to facilitate protein expression.[1] [2] Components of the NPC have been characterized, but how it functions as a complete system has yet to be elucidated. Active transport is facilitated by soluble nuclear transport receptors (NTRs) that shuttle the cargos through the nuclear pore complex. In vertebrates, most active nuclear import of cargos is facilitated by the NTR importin-β karyopherin family.[3] [4] Chapter 3 describes the use of fluorescence recovery after photobleaching (FRAP) and inverse FRAP (iFRAP) to characterize the dynamics of importin-β in the nuclear pore complex.

The NPC is a large superstructure, which is anchored in the nuclear envelope. The pore is comprised of at least 30 types of proteins, which are present in multiples of 8, adding up to several hundred proteins per pore. With a molecular mass of 120 MDa in higher eukaryotes, this molecular machine is among the largest in the cell. The NPC dynamically adapts its structure in response to transport of different types of cargos and regulation of transport selectivity. Chapter 4 describes the use of super-resolution microscopy to characterize the distribution of importin-β in the NPC under a range of conditions and make observations relevant to the kinetics and thermondynamics of importin-β interaction with the NPC.

1.2 - Characterizing RNA-protein Interactions with Plasmon Rulers

Single-molecule imaging techniques have made dramatic progress over the past 15 years. One important advance has been the discovery of large stochastic fluctuations in the catalytic rates of enzyme activity, which diverge from the mean rates observed in bulk experiments.[5]

Single-molecule assays have sought to characterize these fluctuations in catalytic rates by tracking conformational changes in enzyme-substrate complexes as the catalytic reaction progresses to completion. To monitor the spatial shifts of components within these complexes, single-molecule measurement tools, which can be used over with nanometer length scales, have been developed

Forster resonance energy transfer (FRET) between a donor and an acceptor dye has been the preferred method for these types of distance measurements.[6] [7] FRET makes use of the $1/r^6$ dependence of energy transfer between two dyes separated by a distance r. The distance between the two dye molecules can be calculated based on FRET efficiency measurements, which in turn provides information about the spatial conformation of the labeled complex. FRET has been used to characterize molecular motors,[8] [9] RNA ribozymes,[10] and DNA helicases[11] and binding proteins.[12]

However, FRET has limitations in terms of its spatial and temporal scale. Its dynamic range is limited to 1-8 nm[13], and conventional organic dyes used for FRET bleach after emitting approximately10^7 photons[14], limiting observation times to approximately 60 seconds *in vitro*. Additionally, the blinking of FRET dyes adds difficulty to interpretation of single-molecule FRET traces.

These limitations have prompted the development of new tools to make nanometer length-scale measurements and characterize the spatial dynamics of molecular complexes. Plasmon rulers constitute one such tool; they are pairs of noble metal nanoparticles tethered together with DNA, RNA, carbohydrates or proteins. Plasmon rulers have a larger dynamic range than FRET (100nm with 40nm particles). They also do not blink or bleach and can therefore be used to collect single-molecule traces over long timescale imaging. Finally, many such rulers—up to 1000—can be observed in parallel in a single field of view, which dramatically improves data collection efficiency and provides an advantage over other single molecule techniques, such as optical tweezers. This study uses plasmon rulers linked with RNA to study the mechanism of the trp RNA-binding Attenuation Protein (TRAP) in regulating transcription.

RNA-based plasmon rulers were successfully assembled, functionalized, affixed to a flow chamber and imaged in the presence of TRAP protein. However, due to the short persistence length of RNA and the sensitivity limitations of this assay, it was not possible to discern the nanometer length-scale conformational changes in the

RNA during TRAP binding from stochastic fluctuations in RNA conformation due to Brownian motion.

1.3 - Quantifying Dynamics of Importin-β in the Nuclear Pore Complex with FRAP and iFRAP

The nuclear pore complex facilitates transport that is both selective and rapid. The NPC can actively transport cargos up to 40nm in diameter,[15] and yet it can block passive diffusion of cargos as small as 5nm in diameter[16]. The NPC balances this selectivity with speed. It can transport up to 1500 of molecules per second, and larger cargos on the order of 100MDa, can be passed through the pore at a rate of several per second.[17] [18]

Several models have been developed to characterize the molecular mechanism of NPC function, including: the Brownian Affinity model[19], the Affinity Gradient model, the Selective Phase model[20] and the Reversible FG-Domain Collapse model.[21] While these models serve as helpful tools for developing testable hypotheses, they remain the subject of considerable debate, and none have been shown to be categorically correct.

Nuclear transport receptors, such as importin-β, mediate interactions between the cargo and FG-Nups, which line the pore and form a selective barrier to diffusion. To elucidate the nature of this interation, this study characterizes the dynamics of importin-β turnover in the NPC.

Importin-β utilizes a steep RanGTP gradient across the nuclear envelope to shuttle cargos directionally across the NPC. Ran-GTP is maintained at a high concentration in the nucleus, while Ran is found in its GDP-bound form in the cytoplasm. Ran is thought to be necessary for the last step of the active import process—the release of cargo from the NPC into the nucleus.[22] Once the importin-β-cargo complex has traversed the pore to the nuclear face, Ran is thought to bind importin-β, facilitating cargo release into the nucleus. Importin-β is then recycled back to the cytoplasm as part of a complex with Ran, which dissociates upon Ran-GTP hydrolysis. To elucidate some of the mechanistic details of this process, the effects of Ran on importin-β turnover in the pore are characterized.

Nup153 is an FG-Nup that is found on the nuclear face of the NPC and is part of the nuclear basket. In vitro binding affinities of importin-β have been measured, along with those of other FG-Nups in the pore, showing that there is a gradient of binding affinities, which increases along the nuclear pore axis from the cytoplasm to the nuclear basket. Nup153 has been shown to be essential for efficient active import. Active import is dramatically reduced in permeabilized HeLa cells in which Nup153 has been knocked down.[23] Equivalent results have been shown in yeast analogs. This raises the questions: What is the role of Nup153 in import? And does its high

affinity for importin-β and its position within the nuclear basket provide any clues to its function? It has been postulated that there may be a high-affinity site at the exit of the pore, which traps actively transported cargos, and which is the site of a Ran-dependent release step.[24] This model is tested by examining the influence of Nup153 on importin-β dynamics in the pore and the effects of Nup153 and Ran interaction.

New developments in microscopy enable the fast-timescale imaging necessary to capture the millisecond timescale turnover events of importin-β in the pore. Fast wide-field imaging using a custom built microscope enabled imaging at a much faster frame rate than possible in laser scanning confocal microscopy. Real-time FRAP was performed on a custom-built microscope, which allows simultaneous high-speed wide-field imaging with a controlled diffraction limited bleaching spot at the center of the field of view. This is an improvement over laser-scanning confocal imaging approaches, which are limited by the rate at which the imaging laser scans the field of view, making it difficult to image single cell nuclei at a frame rate greater than 10Hz. The wide-field imaging approach used in this study facilitated imaging at 40Hz, making it possible to observe rapid importin-β turnover caused by Ran.

The development of new photoswitching fluorophores (such as mEOS2) has made it possible to examine fluorescence decay through inverse FRAP experiments. GFP-fusion protein expression in live cells has led to dramatic advances in cell biology by enabling the tracking of protein movement in cells with high spatial and temporal resolution. The recent development of photoswitchable fluorescent proteins has made it possible to observe discreet subpopulations of photoswitched molecules and characterize the trajectory of their movement within cells. Irradiation with UV light irreversibly converts these fluorophores from a green to red fluorescent state, which is very bright and photostable. This enables imaging on traditional fluorescence microscopes over long timescales with limited photobleaching. The engineering of monomeric versions of these photoswitchable proteins (such as mEos, Dendra and mKikGR) has precluded the formation of dimers or oligomers, and thus minimized the disruption of normal protein function. This study uses mEOS2-tagged importin-β to perform inverse FRAP (iFRAP) experiments on nuclear pore complexes in the nuclear envelope. By photoswitching a region of the nuclear envelope and monitoring the decay of red fluorescent signal we obtain information about the turnover kinetics of importin-β in the pore.

1.4 - Characterizing the Spatial Distribution of Importin-β with Super-resolution Microscopy

Characterization of the NPC structure is challenging because it is a large complex comprised of at least 30 types of proteins; it is a membrane bound structure; and it dynamically adapts its structure in response to transport of different types of cargo and regulation of transport selectivity.

Much of what is known about NPC structure has been discovered through cryo-electron microscopy studies. Most electron microscopy studies of NPC structure have utilized isolated nuclear envelopes, which have been prepared using detergents, posing the risk of introducing artifacts and undermining confidence that the observed structures accurately reflect the ensemble of *in vivo* states of the pore. However cryo-electron tomography was recently used to characterize the structure of *Dictyostelium* NPC in intact nuclei.[25]

The vertebrate NPC core structure has a 70nm height and a 125 nm diameter. These structures are too small to be resolved with conventional fluorescence microscopy, which has spatial resolution limits of approximately half the wavelength of imaging light—effectively 250-300nm—due to the diffraction of light. Electron microscopy provides much higher resolution, owing to its utilization of 0.01nm wavelength electron beams. However, this method requires the addition of contrast agents and cannot tag specific proteins of interest.

New developments in super-resolution microscopy, such as PALM and STORM have made it possible to overcome the resolution limits of traditional fluorescence microscopy while maintaining the ability to fluorescently tag proteins of interest. Using stochastically activated single fluorophores, point sources of light can be localized with 10nm precision. Composite images that compile hundreds of thousands to millions of localizations can provide high-resolution maps of the distribution of proteins of interest within large structures in the cell.

dSTORM imaging was used to characterize the distribution of importin-β in the NPC with 10nm precision. By obtaining these images at a range of importin-β concentrations, we obtain information about the occupancy of importin-β in the pore. By observing how the distribution changes as a function of concentration we obtain information about the relative *in vivo* binding affinity of importin-β for different regions of the pore.

Custom developed image processing software was used to automate identification and alignment of pores from dSTORM images, thereby avoiding introduction of bias into the analysis. This approach also enhances efficiency of data analysis, making it possible to collect information about large numbers of pores and improve statistics.

1.5 - References

[1] Peters, R., (2006). Introduction to nucleocytoplasmic transport: molecules and mechanisms. *Methods Mol. Biol.* 322, 235–258.

[2] Wente, S.R., Rout, M.P., (2010). The nuclear pore complex and nuclear transport. *Cold Spring Harb. Perspect. Biol.* 2, a000562.

[3] Ohno, M., Fornerod, M. and Mattaj, I. (1998). Nucleocytoplasmic transport; the last 200 nanometres. *Cell* 92, 327-336.

[4] Görlich D., Kutay U. (1999). Transport Between the Cell Nucleus and the Cytoplasm. *Annu. Rev. Cell. Dev. Biol.* 15, 607-660.

[5] van Oijen, A. M., Blainey, P. C., Crampton, D. J., Richardson, C. C., Ellenberger, T., and Xie, X. S. (2003). Single-molecule kinetics of lambda exonuclease reveal base dependence and dynamic disorder. *Science* 301, 1235–1238.

[6] Ha, T., Enderle, T., Ogletree, D. F., Chemla, D. S., Selvin, P. R., and Weiss, S. (1996). Probing the interaction between two single molecules: Fluorescence resonance energy transfer between a single donor and a single acceptor. *Proc. Natl. Acad. Sci. USA* 93(13), 6264–6268.

[7] Ha, T., Ting, A. Y., Liang, J., Caldwell, W. B., Deniz, A. A., Chemla, D. S., Schultz, P. G., and Weiss, S. (1999). Single-molecule fluorescence spectroscopy of enzyme conformational dynamics and cleavage mechanism*. Proc. Natl. Acad. Sci. USA* 96(3), 893–898.

[8] Smiley, R. D., Zhuang, Z. H., Benkovic, S. J., and Hammes, G. G. (2006). Single-molecule investigation of the T4 bacteriophage DNA polymerase holoenzyme: Multiple pathways of holoenzyme formation. *Biochemistry* 45(26), 7990–7997.

[9] Tomishige, M., Stuurman, N., and Vale, R. (2006). Single-molecule observations of neck linker conformational changes in the kinesin motor protein. *Nat. Struct. Mol. Biol.* 13(10), 887–894.

[10] Zhuang, X. W., Kim, H., Pereira, M. J. B., Babcock, H. P., Walter, N. G., and Chu, S. (2002). Correlating structural dynamics and function in single ribozyme molecules. *Science* 296(5572), 1473–1476.

[11] Rasnik, I., Myong, S., and Ha, T. (2006). Unraveling helicase mechanisms one molecule at a time. *Nucleic Acids Res.* 34(15), 4225–4231.

[12] Morgan, M. A., Okamoto, K., English, D. S., and Kahn, J. D. (2005). Single-molecule FRET studies of Lac repressor-DNA loop population distributions. *Biophys. J.* 88(1), 382a.

[13] Lakowicz, J.R. *Principles of Fluorescence Spectroscopy*. (Springer: 1999).

[14] Dubois, A. et al. (1996). Photostability of dye molecules trapped in solid matrices. *Appl. Opt.* 35, 3193-3199.

[15] Pante, N., Kann, M. (2002). Nuclear pore complex is able to transport macromolecules with diameters of about 39 nm. *Mol. Biol. Cell* 13, 425–434.

[16] Keminer, O., Peters, R. (1999). Permeability of single nuclear pores. *Biophys. J.* 77, 217–228.

[17] Ribbeck, K., Gorlich, D. (2001). Kinetic analysis of translocation through nuclear pore complexes. *EMBO J.* 20, 1320–1330.

[18] Siebrasse, J.P., Peters, R. (2002). Rapid translocation of NTF2 through the nuclear pore of isolated nuclei and nuclear envelopes. *EMBO Rep.* 3, 887–892.

[19] Rout, M.P., Aitchison, J.D., Magnasco, M.O., Chait, B.T. (2003). Virtual gating and nuclear transport: the hole picture. *Trends Cell Biol.* 13, 622–628.

[20] Ribbeck, K., Gorlich, D. (2002). The permeability barrier of nuclear pore complexes appears to operate via hydrophobic exclusion. *EMBO J.* 21, 2664–2671.

[21] Lim, R.Y., Fahrenkrog, B., Koser, J., Schwarz-Herion, K., Deng, J., Aebi, U. (2007). Nanomechanical basis of selective gating by the nuclear pore complex. *Science* 318, 640–643.

[22] Lowe, A.R., Siegel, J.J., Kalab, P., Siu, M., Weis, K., Liphardt, J.T. (2010). Selectivity mechanism of the nuclear pore complex characterized by single cargo tracking. *Nature* 467, 600–603.

[23] J. Tang, unpublished results.

[24] Zilman, Anton, Stefano Di Talia, Brian T Chait, Michael P Rout, and Marcelo O Magnasco. (2007). Efficiency, Selectivity, and Robustness of Nucleocytoplasmic Transport. *PLoS computational biology* 3(7), e125.

[25] Beck, Martin, Vladan Lucić, Friedrich Förster, Wolfgang Baumeister, and Ohad Medalia. (2007). Snapshots of nuclear pore complexes in action captured by cryo-electron tomography. *Nature* 449(7162), 611-5.

Chapter 2
Single-molecule study of TRAP Using Plasmon Rulers

2.1 - Summary

This chapter details the study of the role of the trp RNA-binding Attenuation Protein (TRAP) in regulating transcription. In *Bacillus* species TRAP binds messenger RNA and interferes with transcription elongation. The structural changes imposed by TRAP on its target RNA have been characterized as have the bulk binding kinetics. However, the mechanistic details of this process have yet to be elucidated. Single molecule experiments utilizing RNA-linked plasmon rulers are used in an attempt to characterize the mechanism of TRAP binding to RNA.

2.2 - Introduction

Microorganisms are often faced with fluctuating conditions caused by changes in their environment and shifting metabolic demands. Their survival depends on their ability to rapidly alter gene expression in a measured way that helps them continue to function under new conditions. A widely used mechanism for modulating gene expression is the control of transcription initiation, but this is only part of the bacterial regulatory framework.[1] [2] Many mechanisms for regulating transcription elongation have been recently discovered, and up to ten percent of the operons in many bacterial species may be regulated in this fashion through transcription attenuation[3].

The TRAP protein participates in the transcription attenuation mechanism that regulates tryptophan biosynthesis in *Bacillus* species, such as *B. subtilis* and *B.*

stearothermophilus. This is a nuanced system for fine-tuning gene expression in response to a constantly changing environment. TRAP drives a negative feedback loop; when cellular tryptophan concentrations are high, it binds messenger RNA and down-regulates the expression of trp operon genes, which encode the enzymes that comprise the tryptophan biosynthetic pathway[4]. Dynamic rearrangements of RNA secondary structure determine the fate of trp operon expression.[5]

Once transcription has begun, and the RNA polymerase begins to transcribe the trp leader sequence, high cellular tryptophan concentrations (>40μM) activate TRAP, which binds the nascent transcript in a sequence specific manner. TRAP binding prevents the formation of the anti-terminator loop, thereby allowing an overlapping terminator loop to form. This terminator loop causes polymerase dissociation and transcription attenuation. At low tryptophan concentrations TRAP is inactive and does not bind its target RNA, which allows the anti-terminator loop to form and transcriptional elongation to proceed (Figure 1).[6] [7]

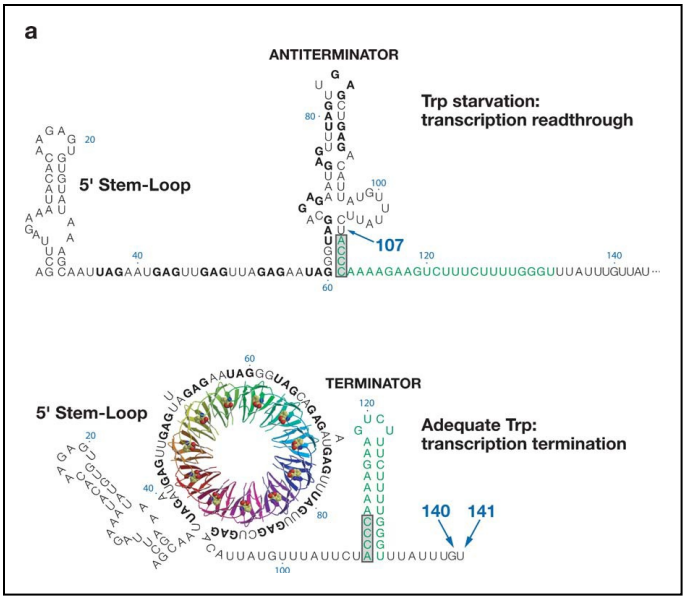

Figure 2.1 - Transcription Attenuation Model.
TRAP binding prevents antiterminator loop formation, thereby inducing terminator loop formation. (Gollnick *et al*. 2005)[5]

TRAP is a ring-shaped, 91 KDa structure comprised of 11 identical subunits. The crystal structure of TRAP bound to RNA shows that active protein associates with its 55-nucleotide binding site, which is comprised of 11 NAG triplet repeats separated by two to three nucleotides of spacer RNA.[8] At saturating tryptophan conditions, RNA is thought to bind WT TRAP in a 5' to 3' direction,[9] winding around the protein in a clockwise fashion. Each TRAP subunit makes direct contact with a triplet repeat by forming multiple hydrogen bonds between residues Lysine 37, Lysine 56 and Arginine 58 and the AG nucleotides in each NAG repeat.[5]

TRAP sensitivity to cellular tryptophan levels is mediated by 11 tryptophan binding pockets located between TRAP subunits. Tryptophan is thought to have a local allosteric effect making the RNA-binding site on neighboring subunits less flexible and thereby competent to bind RNA triplet repeat sites.[10] When TRAP is bound to its full complement of 11 tryptophan molecules, it forms a very stable complex with

RNA with a mean dissociation time greater than 30 minutes (Kd= 0.12nM).[11] Under these saturating tryptophan conditions, the TRAP binding rate is very high; its k_a is estimated from bulk studies to be 7 to 38 x10^6 M^{-1} sec^{-1}. [12]

While the static structure of the RNA-TRAP complex has been elucidated, and binding kinetics have been characterized in bulk, the dynamic mechanism of TRAP associating with its RNA binding site is not known. The prevailing theory is that TRAP associates with RNA in a two-step cooperative process. In the putative first step, TRAP associates with several triplet repeats to form an initiation complex. In the second step, the remaining repeats wrap around the TRAP ring [12].

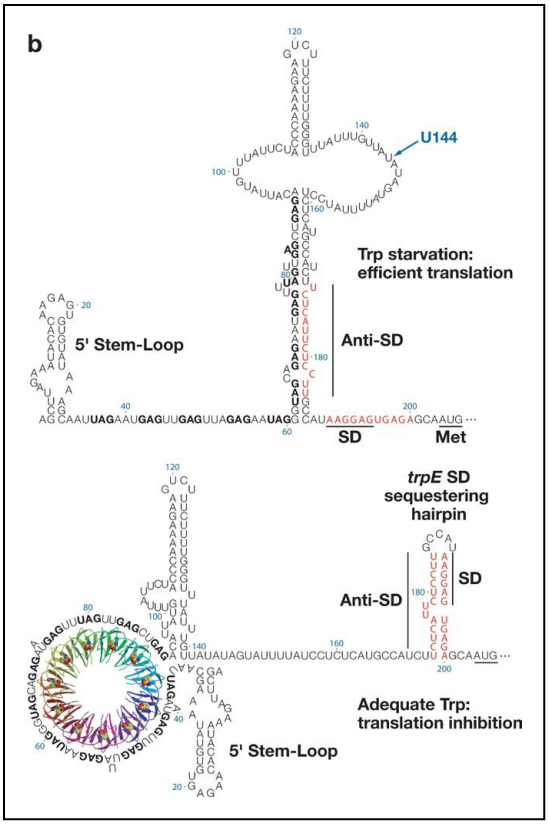

Figure 2.2 – Translation Inhibition Model. TRAP binding induces formation of a hairpin loop that sequesters the Shine-Delgarno sequence. (Gollnick *et al*. 2005)[5]

TRAP binding causes dynamic rearrangements in RNA secondary structure that can influence both transcription elongation and translation. The transcription attenuation mechanism described above causes a 100-fold reduction in trp operon expression. However, TRAP binding to trp leader RNA can also induce formation of a different set of loop structures (Figure 2.2), which disrupt the translation of the first two genes in the trp operon trpE and trpD, by a factor of 15 and 7 respectively.[13] [14]

TRAP binding changes the secondary structure of RNA, inducing the formation of a hairpin loop that sequesters the Shine-Delgarno sequence, which is the ribosome binding site (RBS). In the absence of TRAP binding, a large loop structure forms that keeps the RBS single-stranded and accessible.

These dynamic rearrangements of RNA structure as RNA polymerase generates its transcript invite the question: How does the timing of TRAP binding relative to the polymerase position influence overall expression of the trp operon? At what point must TRAP bind to effectively attenuate transcription or to disrupt translation?

Plasmon rulers can be used to observe the large-scale RNA structural changes that result from TRAP binding. Plasmon rulers are well suited to study the dynamic distance changes involved in these rearrangements, and this technique has been proven to be effective at characterizing the dynamics of macromolecules.[15] [16] [17] Comprised of two noble metal nano-particles linked by biopolymers, such as DNA or RNA, plasmon rulers exploit the distance dependence of plasmon coupling to measure changes in interparticle distances.[18] [19] This technique yields single-molecule trajectories of scattered light intensity as a function of time, which provide information about the distance between the two nano-particles over time as well as the nature of the particle fluctuations. I can use this information to determine when TRAP binds, the rate of binding and mechanistic details about the binding process.

The dynamic range and photostability of plasmon rulers are ideal for the length and time scales involved in TRAP manipulation of RNA secondary structure. TRAP binding causes a 20nm length change in RNA, which exceeds the dynamic range of FRET (1-9 nm),[20] a commonly used technique in single-molecule studies. However, this length scale is well within the range of plasmon rulers (100nm with 40 nm particles).[19] [21] The TRAP-RNA complex is very stable and can stay associated for longer than 30 minutes. Conventional organic dyes used for FRET bleach after emitting approximately10^7 photons,[22] limiting observation times to approximately 60 seconds *in vitro*. Plasmon rulers, by contrast, do not blink or bleach so they can be used to collect data for long periods, such as hours or days. The advantage of this method over optical tweezers is that hundreds of plasmon ruler trajectories can be observed in parallel, instead of one at a time, making data collection much more efficient.

Plasmon Rulers

Plasmon rulers measure distance changes by exploiting the distance dependence of plasmon coupling between pairs of metal nanoparticles. Since the optical properties of the probes in plasmon rulers are based on light scattering, they do not blink or bleach and can be used for imaging over long timescales. A drawback of plasmon rulers is their size, which is much larger than organic dyes. Plasmon rulers are typically constructed using nanoparticles that are tens of nanometers in diameter, as compared to conventional organic dyes, which are typically on the order of 1 nm in diameter. Therefore, the most appropriate applications for plasmon rulers are experiments where a large dynamic range and long probe lifetime outweigh the disadvantages of a larger probe size.

Distance Dependence of Plasmon Coupling

The optical properties of noble metal nanoparticles are defined by particle plasmons, coherent oscillations of the particles' conduction band electrons.[23] The resonance frequency of these plasmons depends on the dielectric function of the metal, the particle's size and shape, the presence of other nanoparticles, and the dielectric constant of the environment.[24] At the resonance frequency, the optical cross section of the nanoparticles reaches its maximum and even weak incident fields induce a large response.

The near-fields of individual metal nanoparticles can interact when two or more nanoparticles approach,[25] [26] [27] shifting the resonance wavelength. The distance-dependence of the resonance wavelength allows nanoparticle pairs to report their separation. In dimers of spherical particles, two coupled plasmon modes can be excited using light: a longitudinal and a vertical plasmon mode. In the longitudinal mode the coupled particle dipoles are aligned in a head-to-tail fashion along the long dimer axis, whereas in the vertical mode the dipoles have a parallel alignment perpendicular to the long axis. As a consequence of the relative orientation of the net dipole moments, the longitudinal plasmon mode red-shifts with decreasing interparticle separation, whereas the vertical mode blue-shifts. Under unpolarized white light illumination, the longitudinal mode is stronger and dominates the spectrum of the coupled dimer; the vertical mode can be resolved if it is selectively excited using linearly polarized light.[28]

The distance dependence of the plasmon coupling has been investigated at fixed interparticle distances with different nanostructures such as spherical,[28] [29] cylindrical,[30] [31] and elliptical nanoparticles.[32]

This technique yields single-molecule trajectories of scattered light intensity as a function of time, which provide information about the distance between the two nano-particles over time as well as the nature of the particle fluctuations. This information can be used to determine when TRAP binds, the rate of binding and mechanistic details about the binding process.

2.3 - Results and Discussion

To observe single-molecule trajectories of TRAP binding its target RNA (Figure 2.3), dimers of 40-nm gold nano-particles were tethered together with single-stranded RNA. The rulers were prepared by linking the two particles with tri-thiolated DNA handles hybridized to a single-stranded RNA linker. The nano-particle surface was passivated with a PEG brush to prevent aggregation. Glass flow chambers were prepared and plasmon rulers and protein was introduced with gravity flow. Biotin molecules attached to one particle affixed one end of the ruler to the flow chamber surface. Dark-field microscopy illuminated by unpolarized white light was used to visualize the rulers and collect movies using a CCD camera. Image processing was performed using a particle-tracking algorithm based on the work of Crocker and Grier. This generated single-molecule traces of scattered light intensity as a function of time (Figure 2.4).

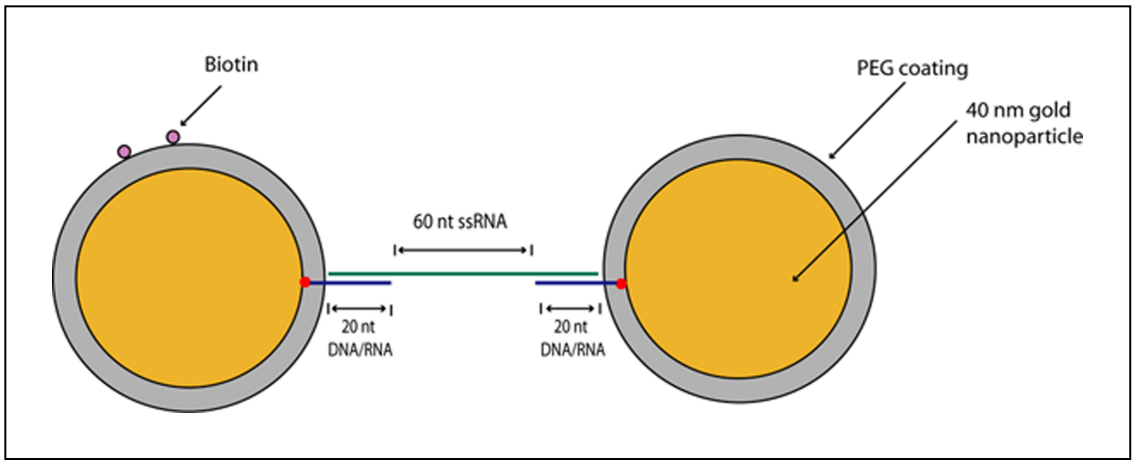

Figure 2.3 –Plasmon Ruler Design. 40nm gold nano-particles linked by single-stranded RNA.

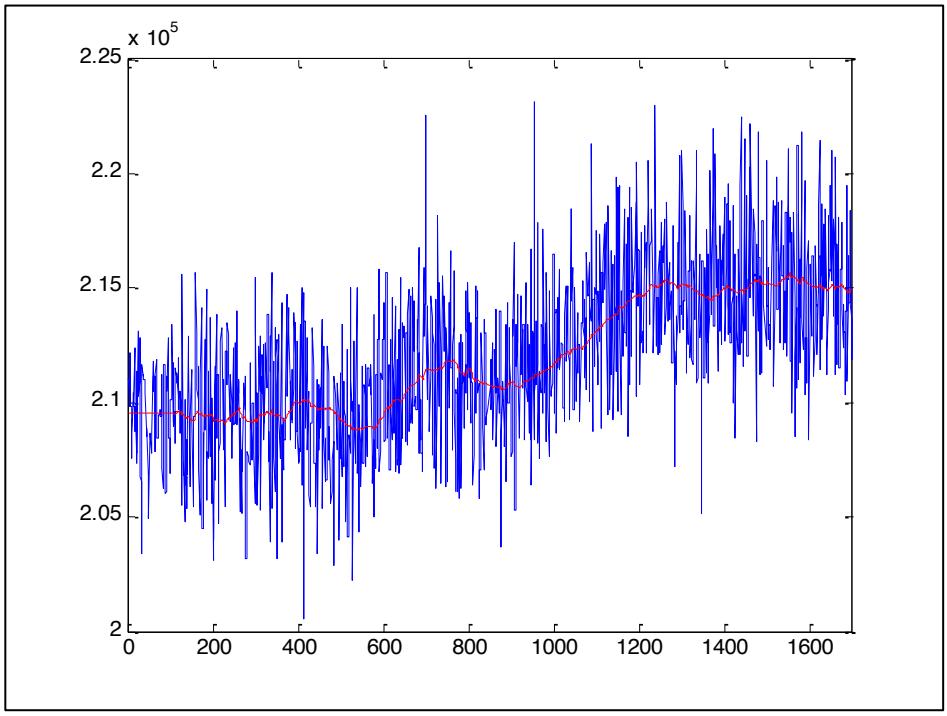

Figure 2.4 – Sample Single-Molecule Plasmon Ruler Intensity Trace. This trace shows intensity of scattered light as a function of time for a single plasmon-ruler trajectory.

In light of the difficulty of observing TRAP-RNA binding events using this technique, we chose not to continue this avenue of study. This difficulty was due to the short persistence length of RNA, such that it was not possible to discern nanometer lengthscale conformational changes in the RNA during TRAP binding from stochastic fluctuations in RNA conformation due to Brownian motion. Simulations of TRAP binding to single-stranded RNA confirmed that the short persistence length

of RNA coupled with the lack of sensitivity of this method undermined our ability to detect binding events.

2.4 – Materials and Methods

Plasmon Ruler Synthesis

The prorietary surface coating on the surface of the gold nanoparticles was replaced with a known chemistry by incubating the particles with in 1 mg/ml bis(p-sulphonatophenyl)phenylphosphine at room temperature (RT) for at least 8 h. Then, these phosphine-passivated particles were functionalized with tri-thiolated ssDNA in a ratio of 1:25 (gold nanoparticle/DNA). Finally, the ssDNA-gold nanoparticles were coated with a monolayer of short polyethylene glycol (PEG) ligands (a 4–8 h RT incubation in thiolated carboxy-terminated PEGs such as thiol-(EG)7-propionate at a ratio of 1:100,000). The PEG ligands are necessary to stabilize the particles in the buffer conditions (80 mM NaCl, 10 mM Tris–HCl, pH 7.0) ultimately required for efficient hybridization. For one of the two types of particles, small amounts of biotinylated PEGs were mixed in with the thiol-PEG–propionate (1:25 ratio) to facilitate immobilization of the assembled dimers to NeutrAvidin functionalized glass surfaces.

A ssRNA tether was synthesized with 5’ and 3’ end sequences that are complementary to the respective DNA handles attached to the gold nanoparticles. The ssRNA tether oligonucleotide was first annealed to one of the particles. After annealing overnight, the particles were thoroughly cleaned through repeated centrifugation and resuspension to remove excess RNA tether oligonucleotides. The cleaned particles were then combined with the second type of nanoparticles that were cleaned in a similar fashion and annealed at RT for several hours. To minimize multiple tether formation during annealing, the tether–particle ratio is limited to 30:1.

After annealing, the assembled dimers were purified and separated from monomers or larger nanoparticle assemblies using gel-electrophoresis, which separates single particles from dimers based on size. This forms a band of dimers, which was cut out of the gel. The particles were then recovered from the gel using electroelution.

Microscopy

The plasmon rulers were observed using dark-field microscopy (Figure 2.5) (Sonnichsen et al., 2000). In dark-field illumination, the excitation light is injected into the focal plane through a dark-field condenser at oblique angles from all directions. The oblique angles do not reach the objective unless they are scattered by an object in the specimen plane. This illumination scheme suppresses the background and enhances the imaging of the nanoparticles with high contrast.

Single particle Rayleigh scattering spectroscopy was performed using an upright microscope (Zeiss Axioplan2) with a 100 W tungsten lamp, oil immersion dark-field

condenser and a 40 objective. The scattered light was analyzed by a CCD detector (Andor iXonEM).

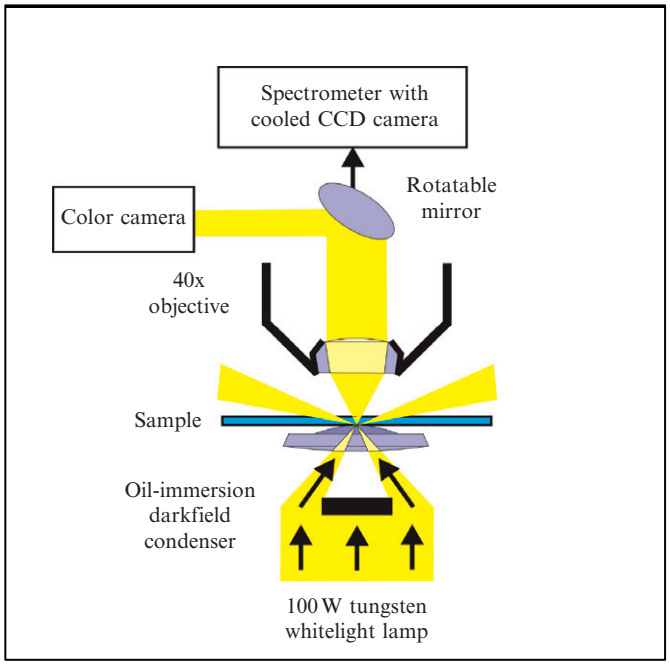

Figure 2.5 Schematic Diagram of a dark-field microscope. Light is injected into the focal plane at oblique angles so that only the light scattered off individual particles in the specimen plane is collected by the objective.

2.5 - References

[1] Winkler, W.C. & Breaker, R.R. (2005). Regulation of bacterial gene expression by riboswitches. *Annu. Rev. Microbiol* 59, 487-517.

[2] Yanofsky, C. (2007). RNA-based regulation of genes of tryptophan synthesis and degradation, in bacteria. *RNA* 13, 1141-1154.

[3] Henkin, T.M. & Yanofsky, C. (2002). Regulation by transcription attenuation in bacteria: how RNA provides instructions for transcription termination/antitermination decisions. *Bioessays* 24, 700-707.

[4] Otridge, J. & Gollnick, P. (1993). MtrB from Bacillus subtilis binds specifically to trp leader RNA in a tryptophan-dependent manner. *Proc. Natl. Acad. Sci. U.S.A* 90, 128-132.

[5] Gollnick, P. et al. (2005). Complexity in regulation of tryptophan biosynthesis in Bacillus subtilis. *Annu. Rev. Genet* 39, 47-68.

[6] Babitzke, P. & Gollnick, P. (2001). Posttranscription initiation control of tryptophan metabolism in Bacillus subtilis by the trp RNA-binding attenuation protein (TRAP), anti-TRAP, and RNA structure. *J. Bacteriol* 183, 5795-5802.

[7] Babitzke, P. & Yanofsky, C. (1993). Reconstitution of Bacillus subtilis trp attenuation in vitro with TRAP, the trp RNA-binding attenuation protein. *Proc. Natl. Acad. Sci. U.S.A* 90, 133-137.

[8] Hopcroft, N.H. et al. (2004). The interaction of RNA with TRAP: the role of triplet repeats and separating spacer nucleotides. *J. Mol. Biol* 338, 43-53.

[9] Barbolina, M.V., Li, X. & Gollnick, P. (2005). Bacillus subtilis TRAP binds to its RNA target by a 5' to 3' directional mechanism. *J. Mol. Biol* 345, 667-679.

[10] McElroy, C. et al. (2002). TROSY-NMR studies of the 91kDa TRAP protein reveal allosteric control of a gene regulatory protein by ligand-altered flexibility. *J. Mol. Biol* 323, 463-473.

[11] Baumann, C., Otridge, J. & Gollnick, P. (1996). Kinetic and thermodynamic analysis of the interaction between TRAP (trp RNA-binding attenuation protein) of Bacillus subtilis and trp leader RNA. *J. Biol. Chem* 271, 12269-12274.

[12] Barbolina, M.V. et al. (2007). The rate of TRAP binding to RNA is crucial for transcription attenuation control of the B. subtilis trp operon. *J. Mol. Biol* 370, 925-938.

[13] Merino, E., Babitzke, P. & Yanofsky. (1995). C. trp RNA-binding attenuation protein (TRAP)-trp leader RNA interactions mediate translational as well as transcriptional regulation of the Bacillus subtilis trp operon. *J. Bacteriol* 177, 6362-6370.

[14] Schaak, J.E. et al. (2003). A Mg2+-dependent RNA tertiary structure forms in the Bacillus subtilis trp operon leader transcript and appears to interfere with trpE translation control by inhibiting TRAP binding. *J. Mol. Biol* 332, 555-574.

[15] Reinhard, B.M. et al. (2007). Use of plasmon coupling to reveal the dynamics of DNA bending and cleavage by single EcoRV restriction enzymes. *Proc. Natl. Acad. Sci. U.S.A* 104, 2667-2672.

[16] Skewis, L.R. & Reinhard, B.M. (2008). Spermidine modulated ribonuclease activity probed by RNA plasmon rulers. *Nano Lett* 8, 214-220.

[17] Reinhard, B.M. et al. (2010). Plasmon Rulers as Dynamic Molecular Rulers in Enzymology. *Methods in Enzymology* 475, 175-198.

[18] Sönnichsen, C. et al. (2005). A molecular ruler based on plasmon coupling of single gold and silver nanoparticles. *Nat. Biotechnol* 23, 741-745.

[19] Reinhard, B.M. et al. (2005). Calibration of dynamic molecular rulers based on plasmon coupling between gold nanoparticles. *Nano Lett* 5, 2246-2252.

[20] Lakowicz, J.R. *Principles of Fluorescence Spectroscopy*. (Springer: 1999).

[21] Jain, P.K., Huang, W. & El-Sayed, M.A. (2007). On the Universal Scaling Behavior of the Distance Decay of Plasmon Coupling in Metal Nanoparticle Pairs: A Plasmon Ruler Equation. *Nano Letters* 7, 2080-2088.

[22] Dubois, A. et al. Photostability of dyemolecules trapped in solid matrices. (1996). *Appl. Opt.* 35, 3193-3199.

[23] Kreibig, U., and Vollmer, M. Optical Properties of Metal Clusters. (Springer-Verlag: 1995), pp. 13–193.

[24] Kelly, K. L., Coronado, E., Zhao, L. L., and Schatz, G. C. (2003). The optical properties of metal nanoparticles: The influence of size, shape, and dielectric environment. *J. Phys. Chem. B* 107(3), 668–677.

[25] Prodan, E., Radloff, C., Halas, N. J., and Nordlander, P. (2003). A hybridization model for the plasmon response of complex nanostructures. *Science* 302(5644), 419–422.

[26] Reinhard, B. M., Siu, M., Agarwal, H., Alivisatos, A. P., and Liphardt, J. (2005). Calibration of dynamic molecular rulers based on plasmon coupling between gold nanoparticles. *Nano Lett.* 5(11), 2246–2252.

[27] Su, K. H., Wei, Q. H., Zhang, X., Mock, J. J., Smith, D. R., and Schultz, S. (2003). Interparticle coupling effects on plasmon resonances of nanogold particles. *Nano Lett.* 3(8), 1087–1090.

[28] Jain, P. K., Huang, W. Y., and El-Sayed, M. A. (2007). On the universal scaling behavior of the distance decay of plasmon coupling in metal nanoparticle pairs: A plasmon ruler equation. *Nano Lett.* 7(7), 2080–2088.

[29] Maier, S. A., Friedman, M. D., Barclay, P. E., and Painter, O. (2005). Experimental demonstration of fiber-accessible metal nanoparticle plasmon waveguides for planar energy guiding and sensing. *Appl. Phys. Lett.* 86(7), 071103.

[30] Haynes, C. L., McFarland, A. D., Zhao, L. L., Van Duyne, R. P., Schatz, G. C., Gunnarsson, L., Prikulis, J., Kasemo, B., and Kall, M. (2003). Nanoparticle optics: The importance of radiative dipole coupling in two-dimensional nanoparticle arrays. *J. Phys. Chem.* B 107(30), 7337–7342.

[31] Rechberger, W., Hohenau, A., Leitner, A., Krenn, J. R., Lamprecht, B., and Aussenegg, F. R. (2003). Optical properties of two interacting gold nanoparticles. *Opt. Commun.* 220(1–3), 137–141.

[32] Wei, Q. H., Su, K. H., Durant, S., and Zhang, X. (2004). Plasmon resonance of finite one-dimensional Au nanoparticle chains. *Nano Lett.* 4(6), 1067–1071.

Chapter 3
Dynamics of Importin-β Interactions with the Nuclear Pore Complex

3.1 – Summary

The nuclear pore complex (NPC) mediates all exchange of materials between the cytoplasm and the nucleus in eukaryotic cells. It is capable of facilitating up to 1500 transport events per second, yet it balances this speed with selectivity. The components involved in this process are known and have been characterized, but how they function as a system remains unclear. FRAP and iFRAP experiments were performed to study the dynamic interactions of importin-β with mammalian NPCs and to characterize the effects of Ran and Nup153 on these interactions.

3.2 - Introduction

The Nuclear Pore Complex

Eukaryotic cells segregate their genetic material into an envelope-bound nucleus, and all transport and communication between these compartments occurs through a large multi-protein channel known as the nuclear pore complex (NPC). NPC-mediated transport of materials between the cytoplasm and the nucleus is essential for many basic cell functions. The NPC selectively imports proteins that are required for DNA maintenance and regulation of gene expression. NPC export of messenger RNA-nucleoprotein complexes to the cytoplasm facilitates protein expression.[1] [2]

Transport through the nuclear pore complex is both selective and rapid. The NPC can actively transport cargos up to 40nm in diameter[3] and yet it can block passive diffusion of cargos as small as 5nm in diameter.[4] The NPC balances this selectivity

with speed. It can transport up to 1500 of molecules per second, and larger cargos on the order of 100MDa, can be passed through the pore at a rate of several per second.[5] [6]

The NPC is comprised of approximately 30 types of nucleoporin proteins (Nups), which are present in multiples of eight, adding up to a total of several hundreds proteins in each pore.[7] [8] These nups are assembled into three concentric layers around the central pore channel. The outermost layer is the 'membrane layer,' which contains Nups that form attachment points between the NPC and the nuclear envelope. The middle layer is called the 'scaffold layer.' One third of the Nups in the NPC comprise the innermost layer and include domains with phenylalanine-glycine repeats, and are therefore referred to as FG-nups. These FG repeat domains protrude into the central pore channel.[9]

Unstructured phenylalanine-glycine repeat (FG-repeat) proteins line the channel to form a selective barrier to diffusion. Transport through the NPC is facilitated by interaction sites on these FG-Nups for complexes of nuclear transport receptors and cargos. The FG domains on FG-Nups contain up to 50 repeats of hydrophobic motifs such as FG, FxFG or GLFG linked with hydrophilic linkers. These FG domains are intrinsically unstructured but may collapse into a folded form upon ligand binding.[10]

The Nuclear Transport Receptor Importin-β

Active transport is facilitated by soluble nuclear transport receptors (NTRs) that mediate interactions between the cargo and FG-Nups within the NPC. The Karyopherin family of proteins is the largest group of transport receptors, with at least twenty types in vertebrates.[11] This study focuses on importin-β, which accounts for most active import in vertebrate cells.

NTRs have multiple FG-Nup binding sites—possibly as many as ten—which suggests that they may form a large binding strip as opposed to several spatially distinct sites.[12] [13] The *in vitro* binding affinities of NTRs to FG domains have been measured with observed Kd values ranging from 10 to 200 nM. [14]

Given that importin-β is present at micromolar concentrations inside mammalian cells under physiological conditions.[15] This suggests that, at equilibrium, the NPC is saturated with importin-β in the absence of other proteins. Thus, importin-β should be thought of as a functional part of the pore as opposed to a soluble interaction partner.

Cargos can be targeted for active import via the NPC with a short peptide sequence that serves as a nuclear localization signal (NLS). Export is facilitated by an equivalent nuclear export signal (NES). For most Karyopherins (Kaps) the NLS or NES interacts directly with the nuclear transport receptor, but sometimes an adaptor protein is required to connect the two proteins. Kaps mediate interaction with the pore through sites that interact with FG repeat domains.[16] [17] Importin-β,

which is the focus of this study, associates with its cognate cargo via the adaptor protein, importin-α (Figure 3.1).

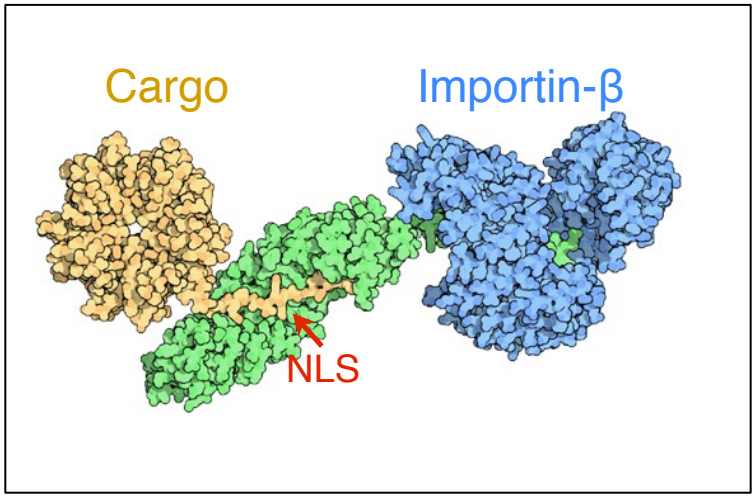

Figure 3.1 - Importin-β complex with adaptor protein and cargo. Actively transported cargo molecules present a nuclear localization signal (NLS) to an adaptor protein, which mediates interaction with importin-β.

Ran Gradient and Directionality of Transport

Receptors of the importin-β karyopherin family utilize a steep RanGTP gradient across the nuclear envelope to carry cargos directionally across the NPC (Figure 3.2). Ran-GTP is present in high concentrations in the nucleus, while Ran is in its GDP-bound form in the cytoplasm. This Ran GTP gradient is maintained by Ran guanidine exchange factor (Ran-GEF) and Ran GTPase activating protein (RanGAP), which are localized to the nucleus and cytoplasm respectively. Ran-GEF is anchored to the chromatin, and it maintains a high nuclear concentration of Ran-GTP.[18] Ran GTPase, which is bound to the cytoplasmic filaments of the NPC in vertebrates, catalyzes the hydrolysis of Ran-bound GTP such that Ran is rapidly converted to its GDP form when exported to the cytoplasm.[19] Cargos with an NLS associate with their cognate Kap in the cytoplasm, where the Ran-GTP concentration is low; the complex traverses the NPC channel; and upon arrival at the nuclear basket, the separation of cargo from its transport receptor is catalyzed by Ran-GTP, which binds to the transport receptor. The Kap-Ran-GTP complex is then returned to the cytoplasm, where it dissociates upon Ran-GTP hydrolysis. The converse of this process uses the same Ran gradient to maintain the directionality of export.[20]

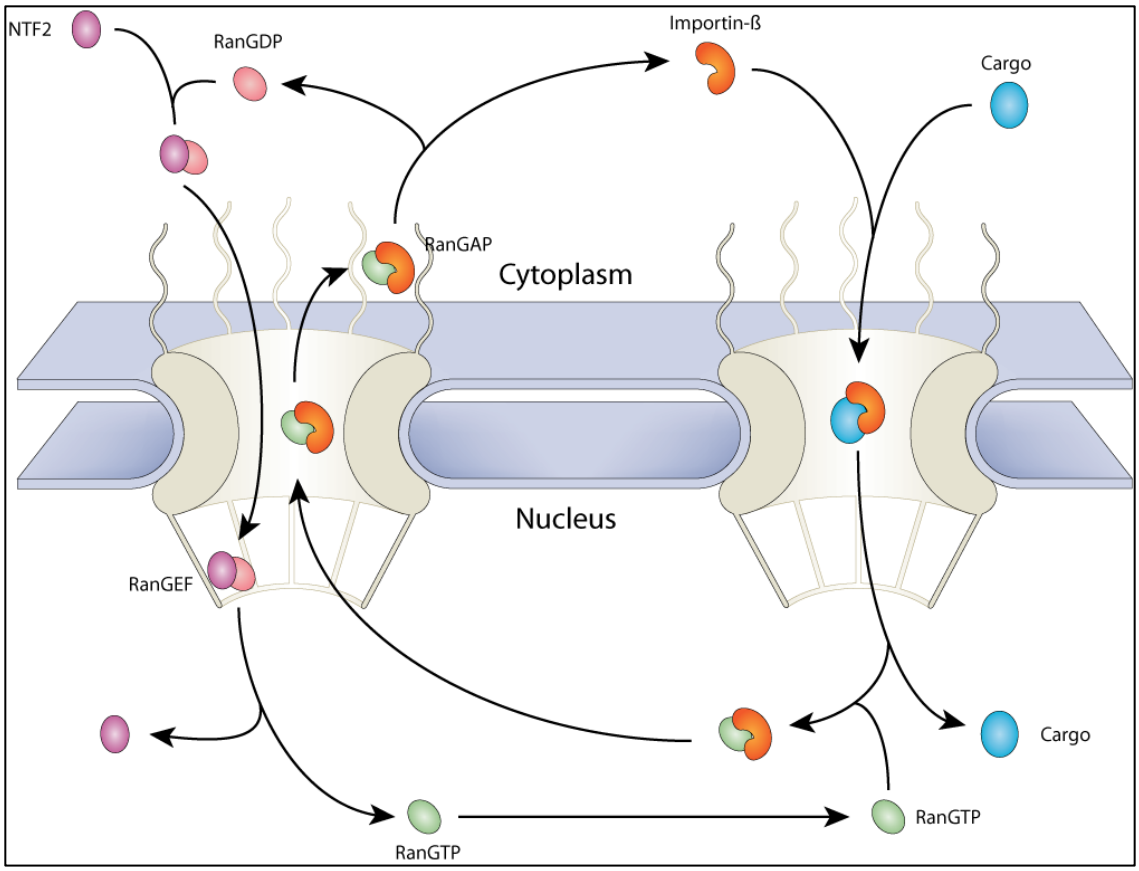

Figure 3.2 - Importin-β mediated active transport and Ran-GTP gradient. The Ran-GTP gradient across the nuclear envelope is maintained by Ran guanidine exchange factor (Ran-GEF), which is anchored to the chromatin; Ran GTPase activating protein (RanGAP), which is attached to the cytoplasmic filaments of the NPC; and NTF2 which cycles RanGDP from the cytoplasm into the nucleus.

Ran-dependence of Import

In a previous study utilizing Snurportin-IBB functionalised Quantum Dot (QD) cargos, it was shown that, in the absence of Ran(+GTP), these large QD cargos explore the entire NPC channel, but have a markedly reduced probability of exit into the nucleus. This suggests that NPC entry and exit steps are not equivalent and that exit from the pore is a ran-dependent process (Figure 3.3).[21]

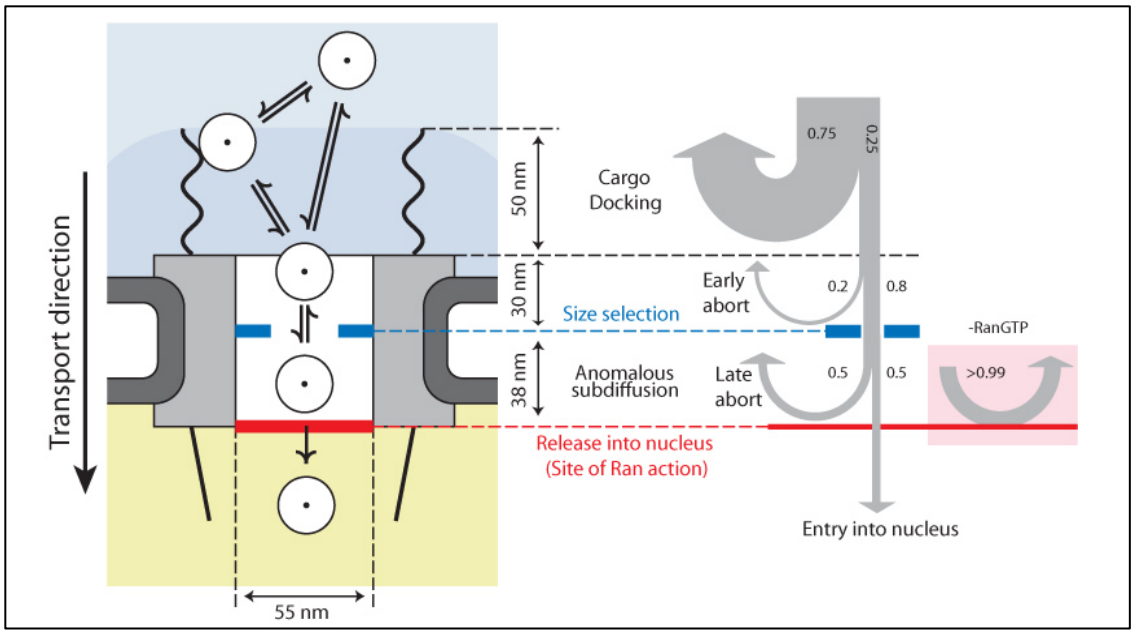

Figure 3.3 - Ran dependence of active import. The final step of active transport, release of cargo into the nucleus, does not take place in the absence of Ran.
(Figure reproduced with permission Lowe *et. al.*, 2010).

Other studies have shown stalling of cargos in the NPC under conditions of energy depletion. The NPC is known to have an asymmetric distribution of FG-repeat containing nucleoporins (FG-Nups) along the channel axis, so the question remains as to why cargos fail to enter the nucleus in the absence of energy. It has been postulated that there may be a high-affinity importin-β binding site at the exit of the pore, which traps actively transported cargos, and which is the site of a Ran-dependent release step. [22]

Importin-β Concentration Dependence of Active and Passive Import

The Ran-driven cargo exit step has been studied by examining the effect of importin-β concentration on active transport of a model cargo (SnurportinIBB-GFP-GFP, ~70 kDa).[23] Nucleocytoplasmic distribution after 15 minutes was analyzed via an established *in vitro* assay using digitonin permeabilised HeLa cells in the presence of recombinant transport factors (importin-β, RanGDP +GTP, and NTF-2) and imaged with fluorescence microscopy. The import efficiency of the model cargo as a function of importin-β concentration was determined in order to identify optimal import conditions (Figure 3.4 b). In the absence of importin-β, no significant import was observed. In the range 0μM<[importin-β]<2μM, efficient transport is observed, with a peak efficiency at ~1μM. Above 2μM a sharp decline in transport efficiency is observed, and active import is severely reduced.

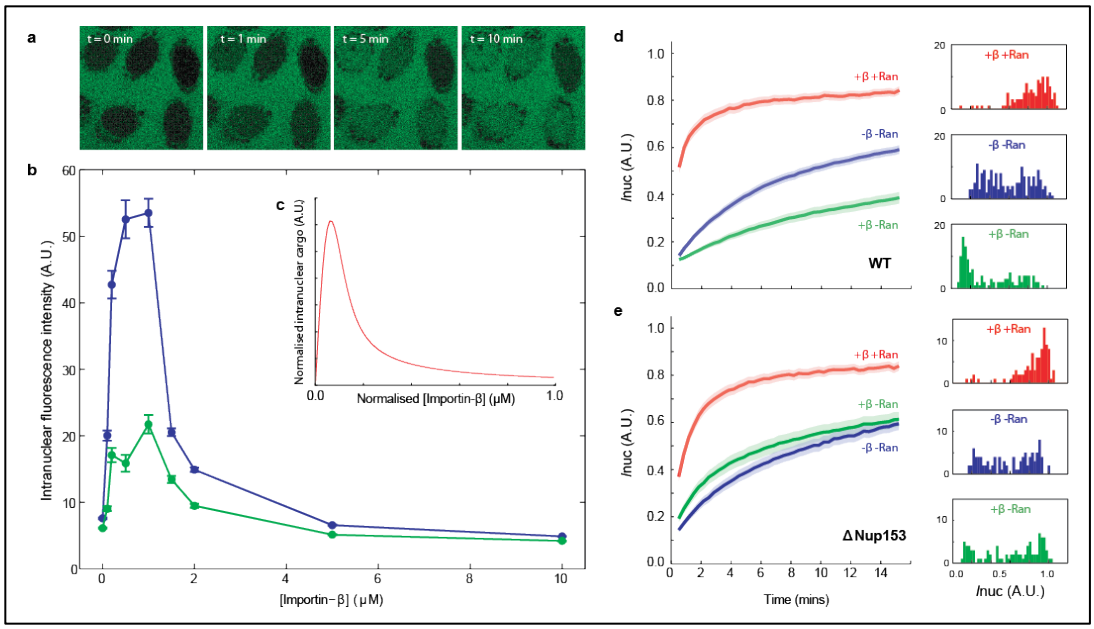

Figure 3.4 - Active and passive transport via the NPC. Active transport of a model fluorescent cargo (Snurportin IBB-GFP-GFP) is mediated by importin-β with peak import efficiency at ~1uM (blue plot). Nup153 RNAi knockdown dramatically decreases import efficiency (green plot) (b). A simple kinetic binding model is consistent with these results (c). Passive import of 2xGFP cargos was observed in the presence and absence of importin-β and Ran in wild-type cells (d) and ΔNup153 cells (e). The traces show the timecourse of import over 15 minutes, and the import endpoints are displayed as histograms. Images of passive import show the equilibration of cargo in the nucleus over ten minutes (a).

Having established the concentration of importin-β that yields optimal active import, the effect on of concentration on passive diffusion as also determined. The passive diffusion cut-off limit of the mammalian NPC is widely accepted to be <70kDa (~9 nm), so a model fluorescent protein containing two repeats of GFP (2xGFP) was used. The 2xGFP protein was able to slowly diffuse into the nucleus over a timescale of minutes. Upon addition of 1uM importin-β, the rate of passive diffusion of 2xGFP is markedly reduced (Figure 3.4 d). However, the addition of Ran+GTP restores the ability of the 2xGFP probe to rapidly enter the nuclei. This suggests that the optimal concentration of importin-β for active transport blocks passive diffusion in the absence of energy. However, Ran addition removes the importin-β induced blockage of passive diffusion.[24]

Based on these results we have developed a model, which posits that the NPC becomes over-loaded with importin-β, potentially reducing total flux through the channel. The occupation of NPC binding sites by importin-β, forms a barrier to diffusion which is alleviated in the presence of Ran-GTP. In this way, importin-β may in fact function as an intrinsic part of the gating mechanism and indeed the pore itself. This occlusion formed by importin-β binding at high affinity sites within the NPC, in the absence of energy, may be responsible for reduced active and passive import, particularly for large cargos.

Nup153 Effects on Active and Passive Import

Nup153 has been shown to localize to the nuclear ring of the NPC, show a high binding affinity for importin-β, and is critical for importin-α/importin-β mediated transport.[25] Active import efficiency was studied in ΔNup153 cells (~70% knockdown efficiency as judged by immunofluorescence). Active import in ΔNup153 cells was diminished for all concentrations of importin-β compared to wild type cells. However, the observed peak in import efficiency occurred at the same importin-β concentration as in wild type cells (~1 uM) (Figure 3.4 b).

A notable feature of the in vitro import assays using fluorescent model cargos is the appearance of a bright rim where the nuclear envelope is located, signifying a higher local concentration of the cargo at the nuclear envelope. This nuclear rim is interpreted as importin-β–cargo complexes docked at the NPC but not exiting the channel. Indeed, the formation of this nuclear rim requires importin-β, and it is especially pronounced when Ran and GTP are excluded. However, in cells where Nup153 expression has been knocked down through RNAi, the nuclear rim is strongly reduced even when Ran and GTP are absent. This result suggests that Nup153 is a major docking site for import complexes responsible for the observation of a rim at the nuclear envelope. Indeed, *in vitro* measurements of importin-β binding affinities for FG-Nups indicate that there is a binding affinity gradient that increases along the transport axis from the cytoplasmic face of the pore to the nuclear basket, where Nup153 is located (Figure 3.5).

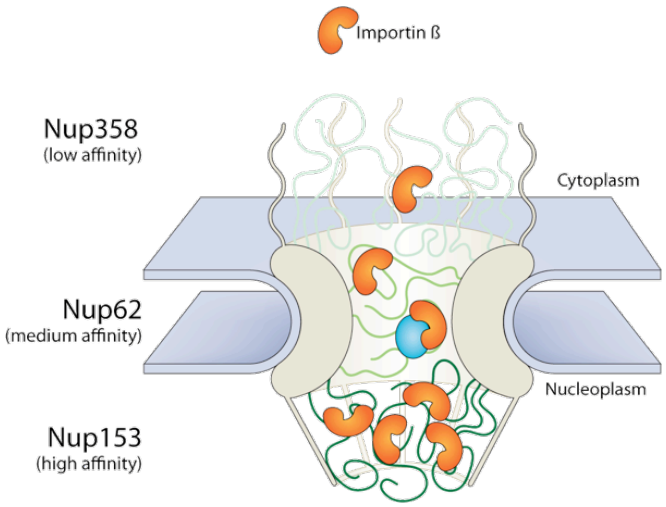

Figure 3.5 - Nup153 high affinity binding site within the NPC. This schematic diagram of the NPC shows the asymmetric distribution of FG-Nups within the pore, based on in vitro binding affinity measurements. An importin binding affinity gradient has been observed with increasing affinity along the import axis from the cytoplasmic face to the nuclear basket.

These observations suggest that importin-β plays an important role in mediating selective active and passive transport in the pore. Importin-β is necessary for import and yet can block it when present at high concentrations. Selective transport may be regulated by a carefully balanced importin-β concentration in the pore, and this balance may be mediated through interactions with Ran-GTP and Nup153.

This invites additional questions about the molecular mechanism of importin-β mediation and regulation of active and passive import. What are the dynamics of importin-β in perform its function? Does it bind FG-Nups within the pore over long timescales, or does it turn over rapidly? How does Ran influence importin-β turnover in the pore, and why do cargos fail to enter the nucleus in the absence of energy? How does Nup153 interact with importin-β and influence its dynamics?

3.3 - Results and Discussion

3.3.1 FRAP

To characterize the millisecond-timescale dynamics of importin-β interaction with the NPC, FRAP experiments were performed to directly monitor the turnover of fluorescently labeled importin-β. This timescale was of interest because import events take place on a milliscond timescale. Permeabilized HeLa cells were treated with 0.1μM YFP- importin-β, in the presence and absence of Ran treatment (a mixture of 5μM Ran-GDP, 1μM GTP and 4μM NTF2). A custom-built fluorescence microscope was used, which utilized a split beam of 514nm laser light. Part of the beam was focused on the sample and used to deliver a 1second bleaching pulse to a small spot on the nuclear envelope. The remainder of the beam, traversed the sample plan in parallel and provided low intensity wide-field illumination. For each experiment, a photobleaching pulse was directed at the nuclear envelope of one cell, and images were collected for 90 seconds at a 40Hz frame rate.

Images were processed using custom written MATLAB code, which automated identification of the cell, nuclear envelope and photoswitched region. The image processing code generated masks for the photoswitched and untreated portions of the nuclear envelope as well as the background (Figure 3.6). These masks were used to extract raw intensity traces for these three regions (Figure 3.7).

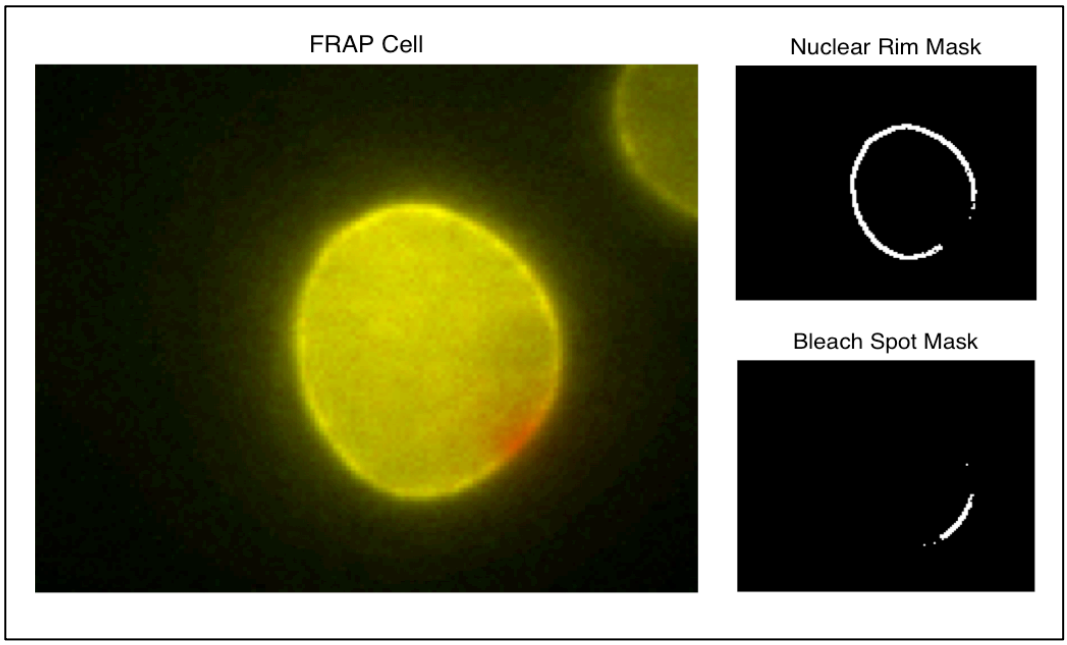

Figure 3.6 - FRAP experiment with YFP-labeled importin-β. The FRAP cell image shows the bright nuclear envelope, comprised of NPCs occupied by YFP-importin-β, and a fluorescent nuclear interior, where imoportin-β has accumulated in the absence of Ran. The image is false colored red to indicate the site of photobleaching. The panels on the right show the identification of the untreated and photoswitched regions of the nuclear envelope.

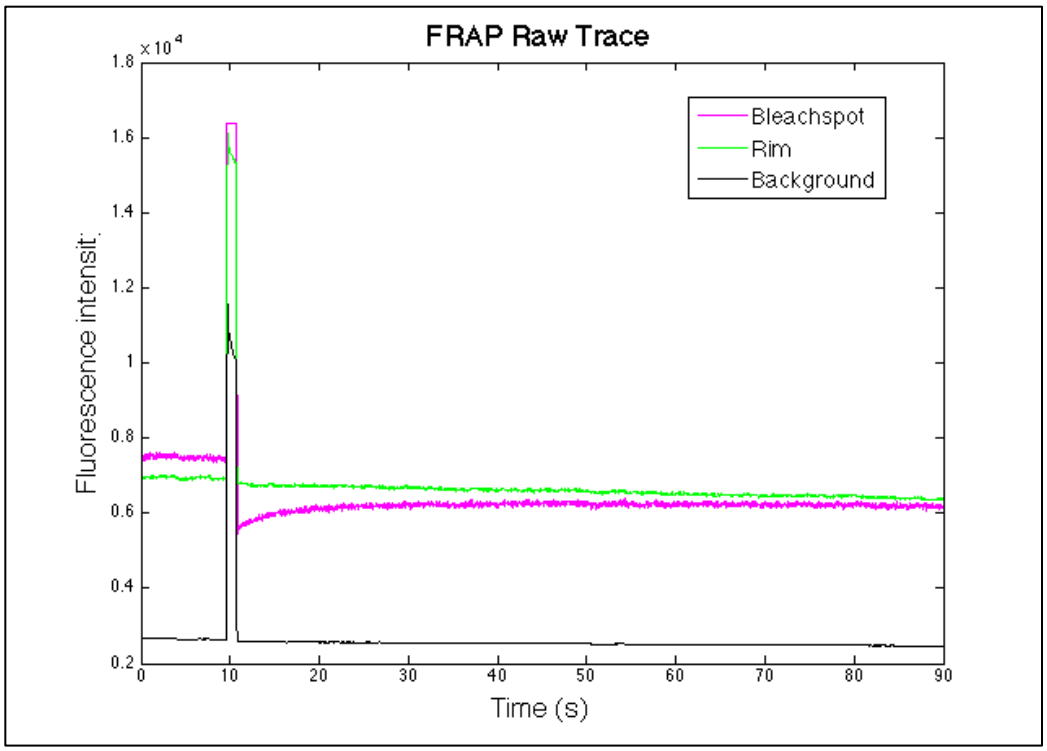

Figure 3.7 - Raw FRAP Intensity Traces. The FRAP experiment produces raw intensity traces of the photoswitched region of the nuclear envelope, the untreated region of the envelope and the background intensity.

Raw intensity traces for the photobleached region of the nuclear envelope were normalized using the untreated portion of the nuclear envelope as a reference. This corrected for bleaching caused by the portion of the 514nm laser beam used to image the sample. The normalization was performed in two steps, using the MATLAB algorithm below (Algorithm 1).

```
%step I – reshape bleach curve
bleach_norm = bleach_mean * ref_pre ./ rim_mean

%reset bleach min after curve reshape
frap_bleach2 = bleach_norm(laser_off);

%step 2- normalize reshaped curve
bleach_norm2 = (bleach_norm - frap_bleach2)./(frap_pre - frap_bleach2);
```

Algorithm 1 – FRAP Trace Normalization. This algorithm used the untreated region of the nuclear envelope as a reference to correct for photobleaching of the nucleus by the imaging laser. The reshaped curve was then normalized based on initial intensity values.

The first step of the normalization uses the untreated portion of the nuclear rim as a reference to reshape the recovery curve to correct for photobleaching by the imaging laser. The second step scales the curve such that the initial pre-photobleach value is set to 1 and the value immediately after the photobleaching pulse is set to zero. Normalized recovery traces were then used to compute mean recovery for each experimental condition.

Ran-associated Fast Recovery Phase

Comparison of mean normalized FRAP recovery traces for importin-β in the presence and absence of Ran show that addition of Ran adds a fast recovery phase which is not observed in its absence. In the presence of Ran a rapid, millisecond timescale recovery phase is observed, and 30 percent of the importin-β population turns over within less than one second of photobleaching (Figure 3.8). This timescale is on the same order as the rate of import events for smaller cargos in the pore. This rapid recovery phase is not observed in the FRAP trace of importin-β in the absence of Ran.

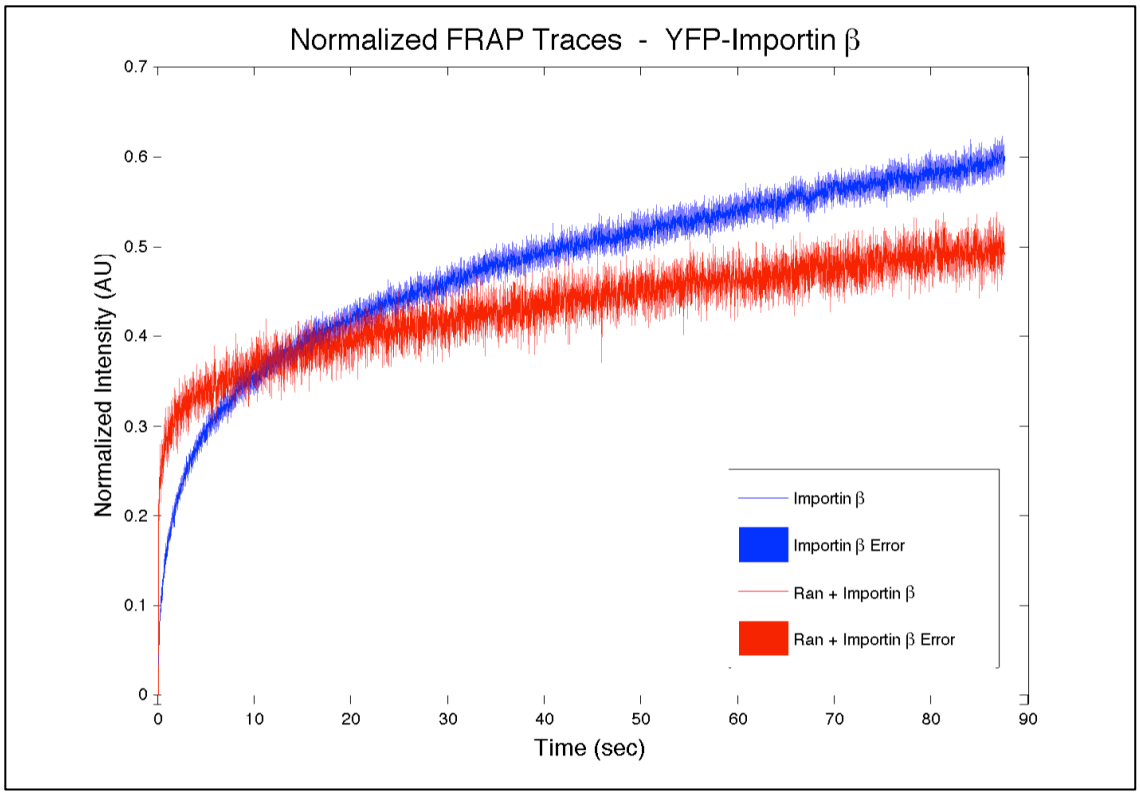

Figure 3.8 - Normalized FRAP Recovery Traces: Importin-β +/- Ran. Mean FRAP traces of Importin-β in the presence and absence of Ran show that Ran yields a fast, millisecond timescale, recovery phase. The standard error of the mean is also shown.

Nup153 Influence on Importin-β Turnover

Similar FRAP experiments were performed to observe the influence of Nup153 on the kinetics of importin-β turnover in the NPC. FRAP experiments were performed on ΔNup153 cells which were knocked down using a two-day RNA interference (RNAi) protocol (70% knockdown efficiency) and wild type control cells that underwent a null RNAi treatment containing all components except the RNA molecules. Comparison of the FRAP recovery traces for importin-β in wild type control cells and ΔNup153 cells suggests that Nup153 knockdown does not change the rates of importin-β turnover in the pore; the shapes of the two recovery traces are the same. However, the reduction of Nup153 in the pore increases the observed fractional magnitude of recovery (Figure 3.9). This is consistent with *in vitro* binding affinity measurements of importin-β, which indicate that Nup153 is a high-affinity binding site within the pore. An explanation for this result is that the removal of high affinity Nup153 sites from the pore, decreases the ratio of high- to low-affinity binding sites within the pore. This leads to a decrease in the fraction of sites occupied by slowly turning over importin-β and an increase in the observed magnitude of normalized recovery.

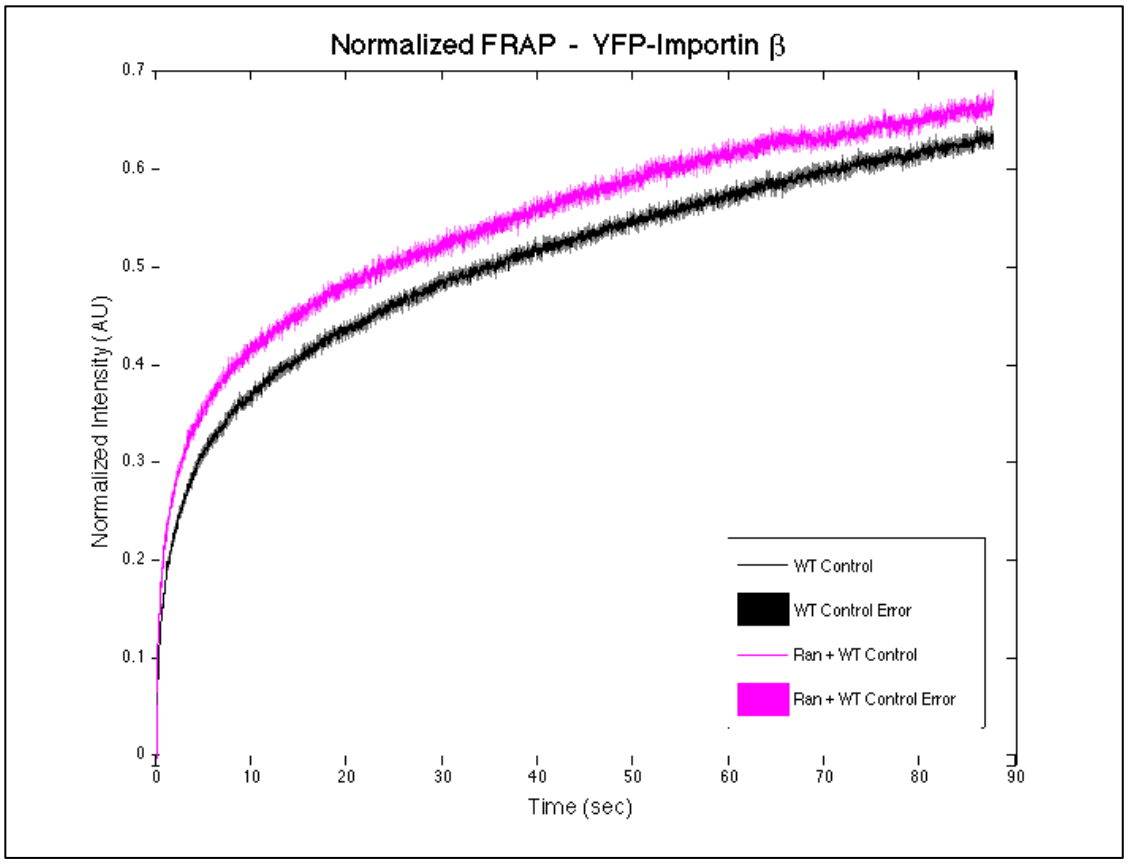

Figure 3.9 - Normalized FRAP Recovery Traces: Importin-β in WT and ΔNup153 cells. Mean FRAP traces of Importin-β in wild type and ΔNup153 cells show that the RNAi knock-down of Nup153 sites increases the amplitude of normalized recovery but does not change recovery rates. The standard error of the mean is also shown.

Bi-exponential Recovery Fitting

The individual normalized recovery traces were fit with a bi-exponential recovery curve (Table 3.1).

$$y(t) = A*(1-exp(B*t)) + C*(1-exp(D*t)) + E$$

The *B* and *D* parameters represent the rate constants; *A* and *C* represent the amplitudes of those rates; and *E* is the value of the curve at T=∞. A single exponential recovery was inadequate to describe the traces, and generated large systematic error. This indicates that there are at least two phases represented in the recorded recovery traces—a fast turnover phase and a slow phase. This interpretation is consistent with the finding that individual NPCs in permeabilized mammalian cells contained two types of importin-β binding sites: a high affinity binding site (effective Kd = 0.3nM) with up to 7 bound molecules per pore, and a low-affinity binding site (Kd = 70nM) with as many as 110 bound molecules per pore.[26]

	WT Beta				ΔN70 Beta	
	-Ran		+Ran		-Ran	
	k1	k2	k1	k2	k1	k2
+Nup 153	3.9 ± 0.5	0.18 ± 0.01	17.1 ± 0.7	0.4 ± 0.05	3.4 ± 0.5	0.07 ± 0.02
-Nup 153	3.5 ± 0.4	0.18 ± 0.01	22 ± 4	0.7 ± 0.5	4.8 ± 0.8	0.1 ± 0.03

	WT Beta				ΔN70 Beta	
	-Ran		+Ran		-Ran	
	A1	A2	A1	A2	A1	A2
+Nup 153	0.139 ± 0.001	0.242 ± 0.009	0.25 ± 0.02	0.117 ± 0.004	0.088 ± 0.06	0.07 ± 0.02
-Nup 153	0.195 ± 0.007	0.256 ± 0.008	0.32 ± 0.03	0.09 ± 0.02	0.099 ± 0.07	0.16 ± 0.03

Table 3.1 – Bi-exponential recovery fits of FRAP traces. Individual FRAP recovery traces were fit with a bi-exponential recovery function.

Long-timescale Importin-β Population

Examination of all the recovery traces described above also suggests that there is a population of importin-β that does not turn over within 90 seconds. Maximal recovery does not exceed 70 percent. This suggests that there is a stable population, which persists in the pore over longer timescales.

Ran-Nup153 Interaction

FRAP experiments were performed with importin-β in the presence of Ran in wild type and ΔNup153 cells. Normalized recovery traces show that Nup153 knockdown decreases the normalized amplitude of recovery in the presence of Ran, but does not change the observed rates (Figure 3.10). This result was somewhat surprising since the knockdown of Nup153, has the opposite effect in the absence of Ran; the knockdown increases the amplitude of normalized recovery in the absence of Ran (Figure 3.9). One possible explanation for this observation is that Ran preferentially acts on importin-β that is bound to Nup153 and that the removal of Nup153 sites reduces Ran activity. Nup153 has a putative Ran binding site.

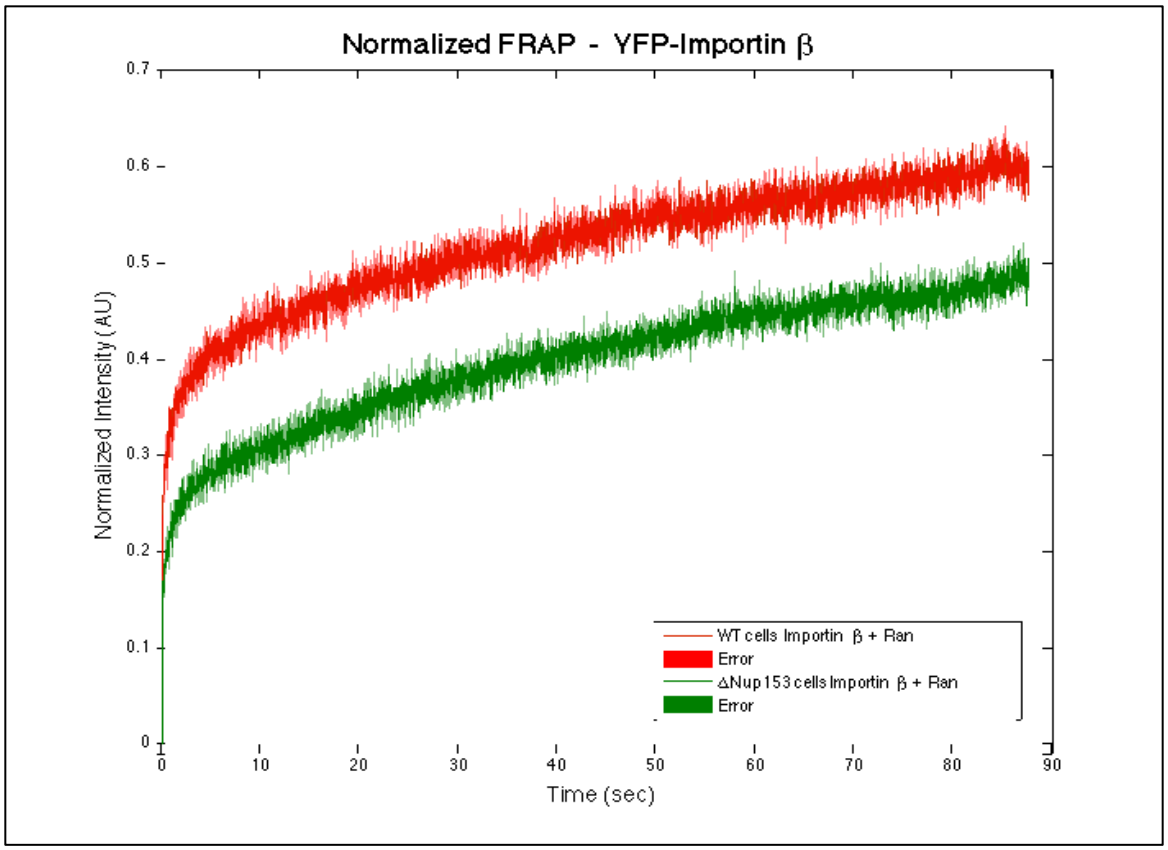

Figure 3.10 - Normalized FRAP Recovery Traces: Importin-β + Ran in WT and ΔNup153 cells. Mean FRAP traces of Importin-β + Ran in wild type and ΔNup153 cells show that the RNAi knockdown of Nup153 sites decreases the amplitude of normalized recovery but does not change recovery rates. The standard error of the mean is also shown.

ΔN70 Importin-β

FRAP experiments were performed with a ΔN70 importin-β mutant. The first 70 amino acids on the N-terminal of importin-β constitute the Ran binding site, and these experiments were conducted with the aim of clarifying the role of Ran in modulating importin-β dynamics in the NPC. The observed recovery amplitude for the ΔN70 mutant was dramatically lower than that of wild type importin-β in the absence of Ran (Figure 3.11). Therefore, deleting the N-terminus of importin-β has additional effects on its interaction with the NPC beyond preventing Ran binding.

It has been shown that similar N-terminal deletions of importin-β prevent active import of cargos and cause the cargo to accumulate within the NPS at the nuclear envelope.[27 28] The observation that the ΔN70 importin-β mutant has an apparent high affinity for the NPC and does not turn over, along with the observation that this mutant prevents active import, suggests that importin-β turnover is essential for active import.

Surprisingly, adding Ran to this mutant importin-β increases normalized recovery amplitude, despite the fact that the Ran binding site has been deleted. There are several possible explanations for this result. If may be due to the increased turnover of residual endogenous wild type importin-β in the nucleus, which was not fully removed during the cell permeabilization procedure. If this were the case, Ran would act on this pool of importin-β and increase its off rate from the NPC. This would make more binding sites available for the fluorescently labeled mutant importin-β but would not change the observed turnover rates of the mutant. This is consistent with the observation that the amplitude of recovery increases, but the curve shapes do not change. Another possible explanation is that Ran is acting on the pore itself, possibly reshaping the FG-Nups and changing their interaction with importin-β. It is not possible to discern which explanation is accurate based on the available evidence. The amplitude of recovery also increases when Nup153 is knocked down. This result is similar to the observation with the equivalent experiment using wild type importin-β (Figure 3.9) and is likely a result of the reduction in high-affinity binding sites.

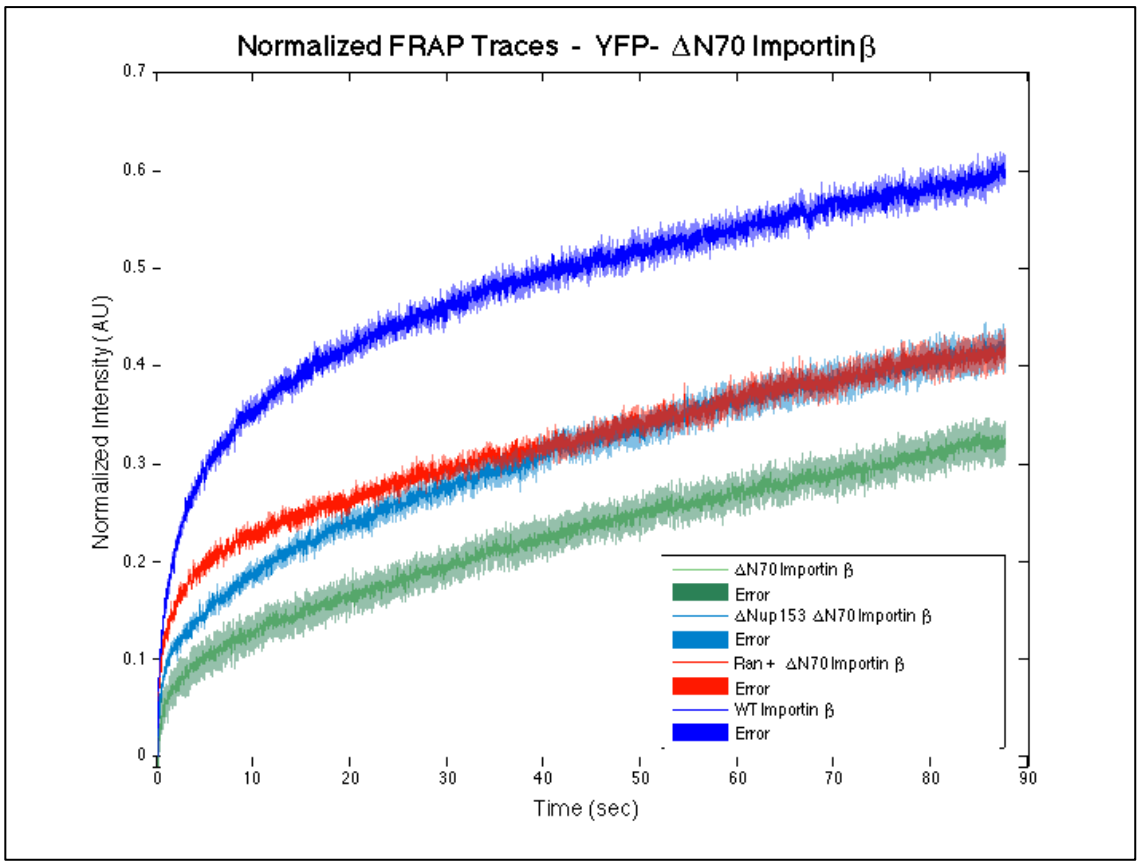

Figure 3.11 - Normalized FRAP Recovery Traces of ΔN70 Importin-β. The recovery amplitude of ΔN70 Importin-β is dramatically lower than that of wild type importin-β. Adding Ran increases ΔN70 importin-β recovery amplitude, as does the RNAi knockdown of Nup153. Mean recovery traces are shown along with standard error of the mean.

FRAP Summary

This set of FRAP experiments yields four key observations. First, Ran introduces a very rapid phase to importin-β recovery in the NPC, suggesting that Ran actively turns over importin-β on a millisecond timescale. Second, the recorded FRAP recovery traces comprise at least two populations of importin-β: a rapidly turning over phase and a slow turnover phase, representing importin-β populations that are bound with low and high affinity respectively. Third, ΔNup153 and wild type cells yield similar FRAP recovery rates, but importin-β has greater normalized recovery amplitude in ΔNup153 cells. This can be explained by the reduction in high affinity binding sites with the knockdown of Nup153. Finally, these FRAP experiments suggest that there may be a residual population of ΔNup153, since at least 30 percent of importin-β do not turn over after 90 seconds.

To verify the existence of this possible slow turnover phase and to examine it in greater detail, longer timescale experiments were necessary. Additional experiments were also required to confirm that there was an observable difference in importin-β dynamics between wild type and ΔNup153 NPCs, since the observed difference in the FRAP experiments described above was small.

3.3.2 - Inverse FRAP (iFRAP)

To observe the turnover of importin-β in the NPC over longer timescales, inverse FRAP (iFRAP) experiments were performed. Permeabilized HeLa cells were treated with 0.1μM fluorescently labeled importin-β. This concentration is approximately 10-fold lower than physiological concentration but was determined to be the optimal concentration for imaging. Importin-β was labeled with the photoswitchable fluourophore mEOS2, which converts from a green to red fluorophore upon activation with 405nm laser light. A Zeiss 700 laser scanning confocal microscope was used to image the cells and photoactivate small segments of the nuclear envelope. The nuclei were imaged in the green (488nm) and red (555nm) channels at 5-second intervals for 5 minutes (Figure 3.12).

Images were processed using a custom-written MATLAB script that locates the cell in the field of view and creates a mask for the region corresponding to the nuclear envelope, the photoswitched region of the envelope, and the nuclear interior (Figure 3.12).

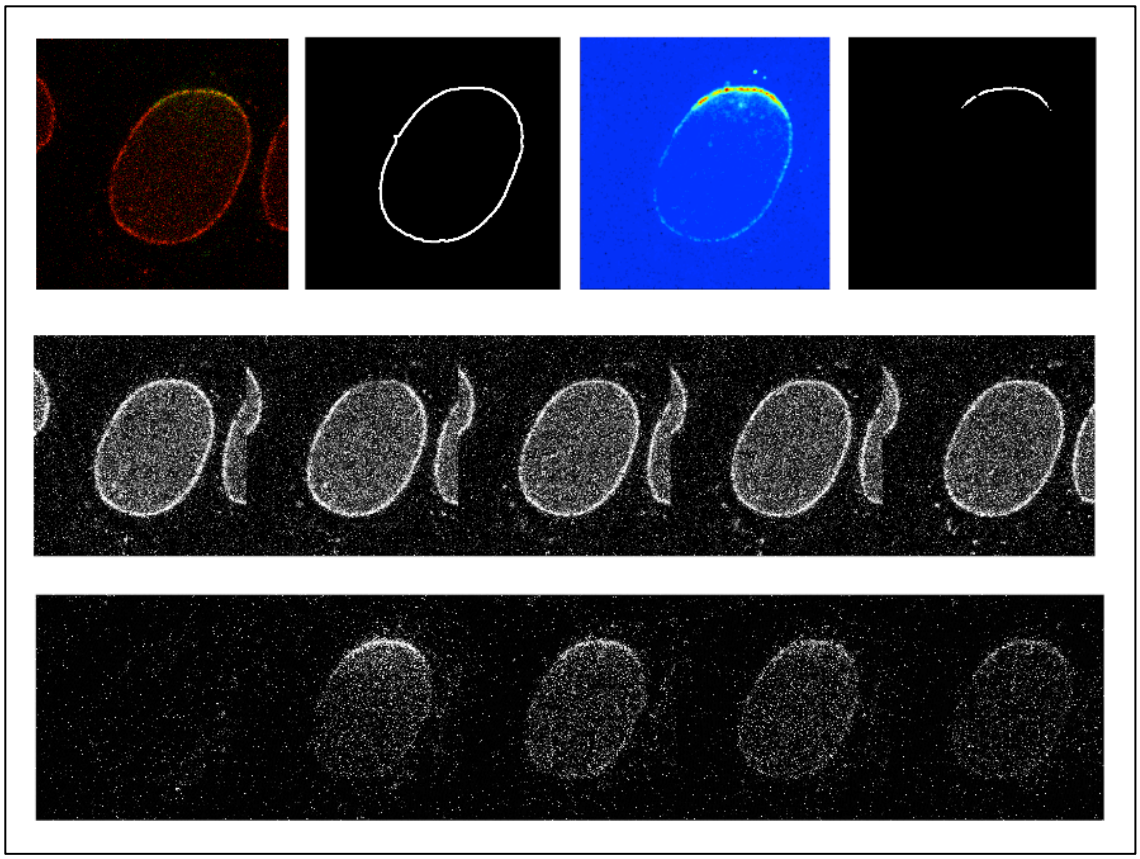

Figure 3.12 – Inverse FRAP Experiment. The top row of images show from left to right: a false-colored image of the nucleus with the photoswitched region indicated in green; the mask generated for the nuclear envelope; a scaled image of the photoswithed region; and a mask for the photoswitched region of the nuclear envelope. The middle panel shows a timecourse of images in the green channel at time points: pre-photoswitch, 0, 50, 100, and 300 seconds. The bottom panel shows a corresponding timecourse of photoswitched molecules in the red channel.

The masks for the photoswitched region of the nuclear envelope and the nuclear interior were used to compute the mean intensity in these regions in both channels at each time point. These data were used to record intensity traces for the photoswtiched region and nuclear interior in the red and green channels (Figure 3.13). The red channel trace for the photoswitched region has a baseline value at background levels for the first four time points, which are followed by the 405nm photoactivating laser pulse. In frame number 5, the intensity increases due to the photoconversion of mEOS2 and decays over time as the photoswitched molecules diffuse away from the pores in that region of the nuclear envelope. The green channel trace for this region has a corresponding decrease in intensity after photoconverstion and recovers over time as the photoswitched molecules diffuse away and are replaced by new green fluorescent importin-β molecules. These two traces provide quantitative information about the kinetics of importin-β turnover in the pore.

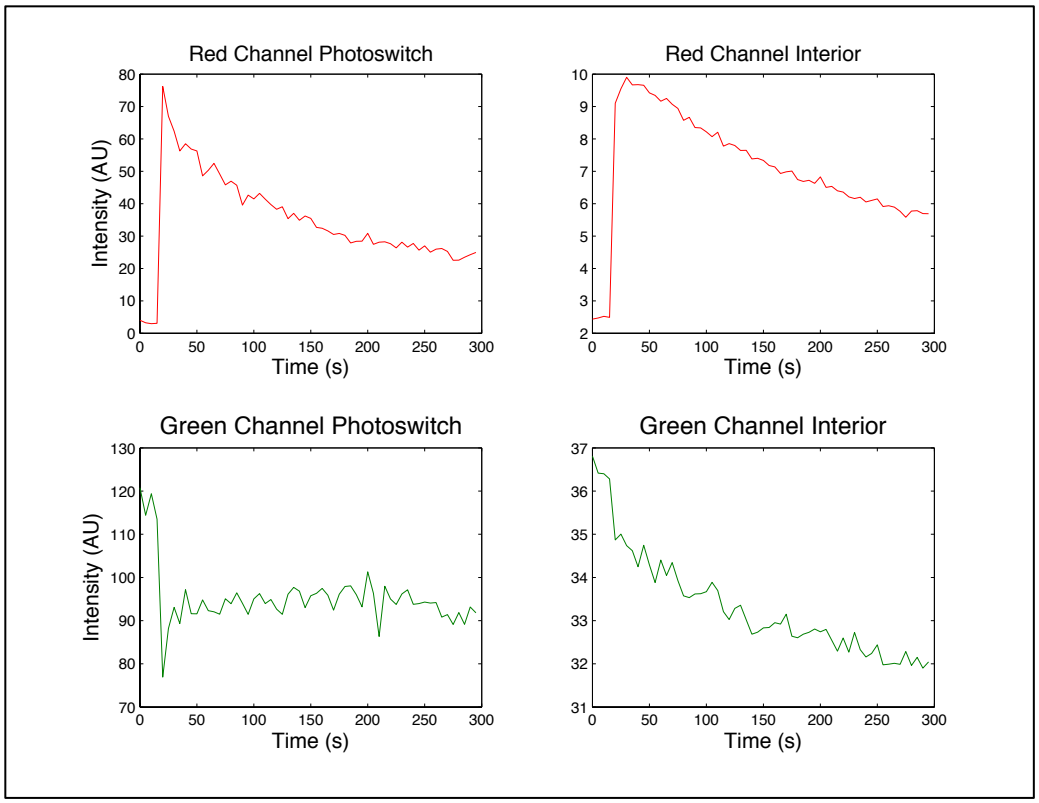

Figure 3.13 – iFRAP Experiment Raw Data. The FRAP experiments generate raw intensity traces of the photoswitched region of the nuclear envelope in the red and green channels (left two panels). Intensity traces for the nuclear interior are also generated for both channels (right two panels).

These experiments were performed under three conditions: wild type cells treated with importin-β, wild type cells treated with importin-β + Ran, and ΔNup153 knockdown cells treated with importin-β (Figure 3.14). The raw intensity traces for the photoconverted region of the nuclear envelope were used to generate mean traces for each of these three experimental conditions. These traces of the decay of red fluorescent signal provide quantitative information about turnover of importin-β in the NPC and the effects of Ran and Nup153 on these dynamics (Figure 3.15).

Observations of Nuclear Rim and Nucleoplasm Fluorescence Intensity

Before discussing the intensity traces described above it is informative to take note of some of the qualitative differences between the three conditions characterized by these experiments. These differences are apparent in images from the green channel (Figure 3.14). In the importin-β condition, the nuclear envelope is brighter than the other two conditions. The nuclear interior is also fluorescent, indicating that importin-β has accumulated in the nucleus. In the importin-β +Ran case the nuclear envelope appears dimmer, indicating that less importin-β is accumulating in the NPC under this condition. The nucleus interior is considerably darker than in the absence of Ran, which can be explained by the fact that Ran-GTP binds importin-β

and recycles it out of the nucleus, as explained above (Figure 3.2). In the ΔNup153 condition, the nuclear envelope is dim, which suggests that fewer importin-β molecules bind to the NPC when those FG-Nups are knocked down. However, the nuclear interior is bright, indicating that importin-β has accumulated in the nucleus. These observations are consistent with the analogous results (described earlier) that were obtained by examining the behavior of fluorescent model cargos in wild type and ΔNup153 cells.[29]

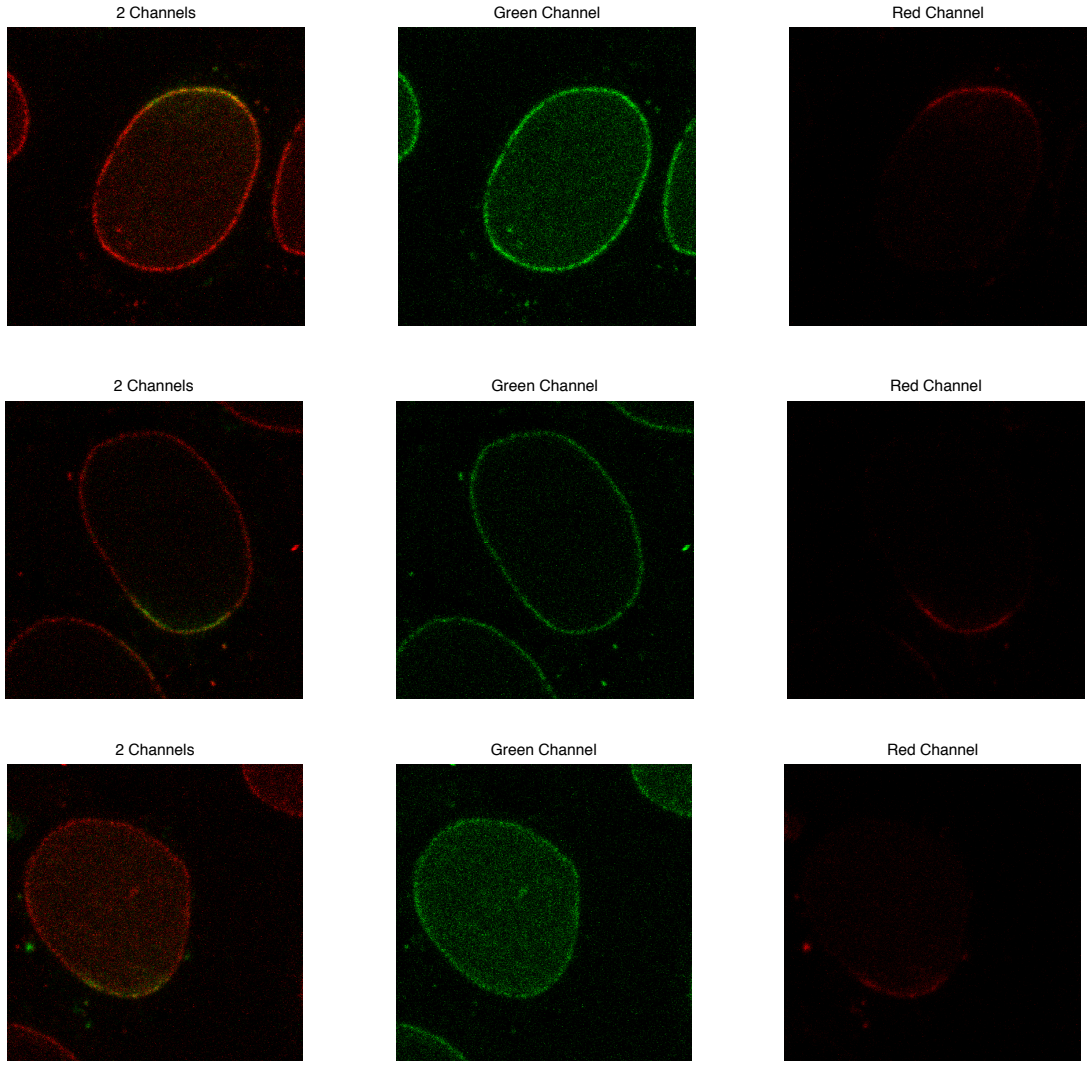

Figure 3.14 – Three experimental conditions. The top row of images corresponds to wild type cells treated with importin-β. The second row shows wild type cells treated with importin-β + Ran. The third row shows and ΔNup153 knockdown cells treated with importin-β. The left column shows a false-colored image of the nucleus with the photoswitched region indicated in green. The middle and right columns respectively show a green channel image of the nucleus before the photoswitching laser pulse, and a red channel image of the nucleus immediately after photoswitching.

The raw intensity traces for the photoconverted region of the nuclear envelope were used to generate mean traces for each of these three experimental conditions. These traces of the decay of red fluorescent signal provide quantitative information about turnover of importin-β in the NPC over a 5-minute timescale, and the effects of Ran and Nup153 on these dynamics (Figure 3.15).

Long-timescale Importin-β Population

The observed fluorescence intensity decay traces do not return to zero, but plateau, suggesting that there is a population of importin-β which turns over very slowly and remains in the pore over long timescales—on the order of minutes or longer (Figure 3.15). Based on curve fitting of these traces (Table 2.3), more than 30 percent of importin-β is estimated to not turn over. This slow turnover population was also observed in a separate set of iFRAP experiments, which collected similar data over 15-minute timescales at 30-second intervals (Appendix I). This result is also strikingly consistent with FRAP experiment results described above, which also show a residual population (>30%) of importin-β in the pore that turns over very slowly (Figures 3.8-3.11). The presence of such a slowly turning over population of is somewhat surprising given that cargo import events have been measured to take place on millisecond timescales.

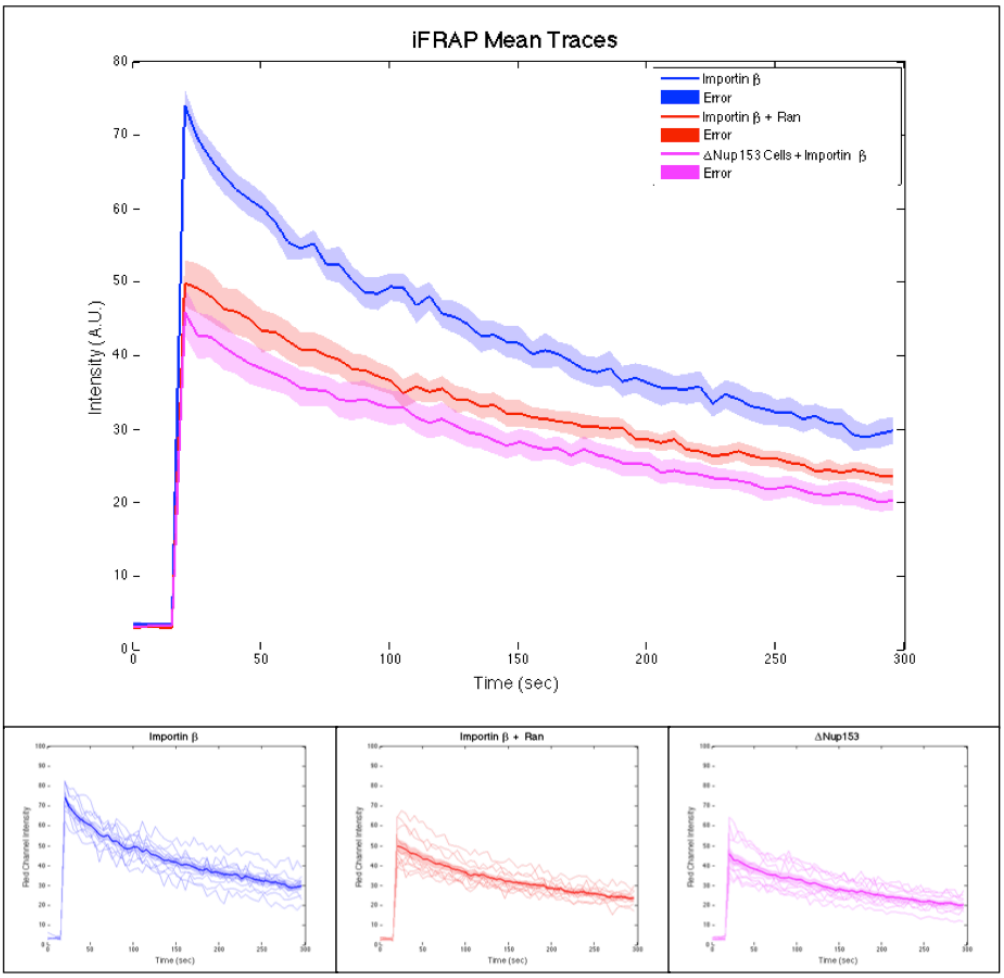

Figure 3.15 – Inverse FRAP Fluorescence Decay Traces. Mean iFRAP traces plotted with standard error of the mean are shown for three experimental conditions: importin-β in wild type cells , importin-β + Ran in wild type cells, and importin-β in ΔNup153 cells. The raw data used to generate these mean traces are shown in the bottom panels.

Initial Intensity Values

In the Ran and ΔNup153 conditions lower initial intensity values are observed immediately after the photoswitching event. The initial intensity of the +Ran condition is approximately 70% of the initial intensity in the absence of Ran (Table 3.2). This could be explained by Ra reducing the affinity of importin-β for FG-Nups within the pore, such that the steady state population of importin-β is decreased. The Ran-induced reduction of importin-β affinity for the pore is consistent with the FRAP results described above in which the introduction of Ran generates a fast phase in importin-β recovery; approximately 30% of the importin-β population turns over on a millisecond timescale (Figure 3.8)—possibly as a result of Ran increasing the off rate of importin-β.

The lower initial intensity values observed in the ΔNup153 condition could indicate lower importin-β occupancy of the pore as a result of removal of high-affinity Nup153 binding sites. This result also reinforces the FRAP experiment observation that there is a difference in the behavior of importin-β in the pore in ΔNup153 cells as compared to WT cells (Figure 3.9).

	Initial Intensity (A.U.)					
	Red Channel			**Green Channel**		
Importinβ	74	±	2	103	±	3
Importinβ + Ran	50	±	3	59	±	4
ΔNup153 cells + Importinβ	46	±	3	69	±	3

Table 3.2 - Initial Fluorescence Intensity Values. Initial intensity values of the photoswitched nuclear envelope region immediately after photoswitching are shown for the red channel. Intensity values for the corresponding region prior to photoswitching are shown in the green channel.

Mean traces for the decay of photoswitched importin-β were generated for the three experimental conditions, and those traces were fit with single and double exponential decay equations. The fits as well the residuals are shown below (Figures 3.16-3.18).

Single exponential decay: $y = (A \times e^{-Bt}) + C$

Double exponential decay: $y = (A \times e^{-Bt}) + (C \times e^{-Dt}) + E$

For the single exponential decay, B is the rate, A is the magnitude, and C is the value at T= ∞. For the double exponential decay B and D are the decay rates, A and C are their respective magnitudes, and E is the value at T= ∞.

For the importin-β trace a single exponential decay fit leaves large systematic error, indicating that this equation is inadequate to characterize these data. However, a bi-exponential fit dramatically reduces the error, suggesting that at least two phases are necessary to describe the turnover of importin-β within the pore under these conditions (Figure 3.16).

When Ran is added to importin-β, and the resulting mean intensity trace is fit with a single exponential decay, there is no systematic error (Figure 3.17). Likewise with the ΔNup153 trace, a single exponential fit has very little systematic error (Figure 3.18). This suggests that importin-β turnover can be described with a single phase under both these conditions. Thus it appears that both of these treatments remove a phase in importin-β turnover.

Examining the mean traces shows that the Ran and ΔNup153 conditions have very similar decay traces, which have a different shape than the importin-β trace. This

observation raises the question of to why these two conditions seem to exhibit similar behavior. One possible explanation is that Ran preferentially turns over importin-β that is bound to Nup153—as opposed to other FG-Nups within the pore—and that the turnover of importin-β at this site accounts for the fast, millisecond timescale turnover phase observed in the FRAP experiments described above (Figure 3.8). Since this phase is too rapid to be detected in longer timescale iFRAP experiments, there is only one remaining observable phase in the turnover of importin-β. In the ΔNup153 case, most of the Nup153 binding sites have been removed, such that the same phase is removed under this condition. The same set of binding sites are left behind in the Ran and ΔNup153 cases, producing similar decay traces. To test this hypothesis, the next logical experiment would be an iFRAP experiment with importin-β + Ran in ΔNup153 cells. If this hypothesis is accurate, the mean iFRAP decay curve of importin-β + Ran in ΔNup153 cells should be very similar to the Ran and ΔNup153 traces.

The preferential action of Ran on Nup153-bound importin-β would also explain the FRAP result that knockdown of Nup153 reduces the magnitude of importin-β recovery in the presence of Ran (Figure 3.10). If the fraction of Importinβ/FG-Nup complexes that Ran can act on is reduced, this would explain the reduced recovery amplitude as compared to the same condition in wild type cells.

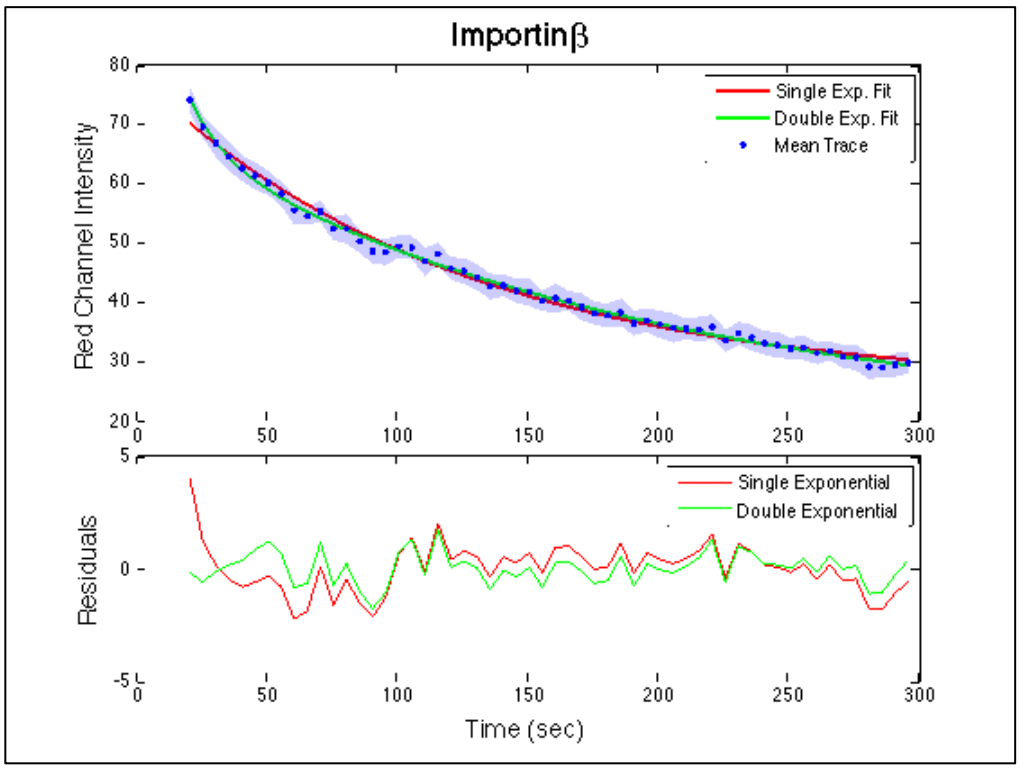

Figure 3.16 – Exponential Fit of Importin-β iFRAP Trace. The mean Importin-β iFRAP trace was fit with single and double exponential decay functions. The fits are shown in the top panel, and residuals are plotted in the bottom panel. The single-exponential fit generates systematic error, which is not observed with a bi-exponential fit.

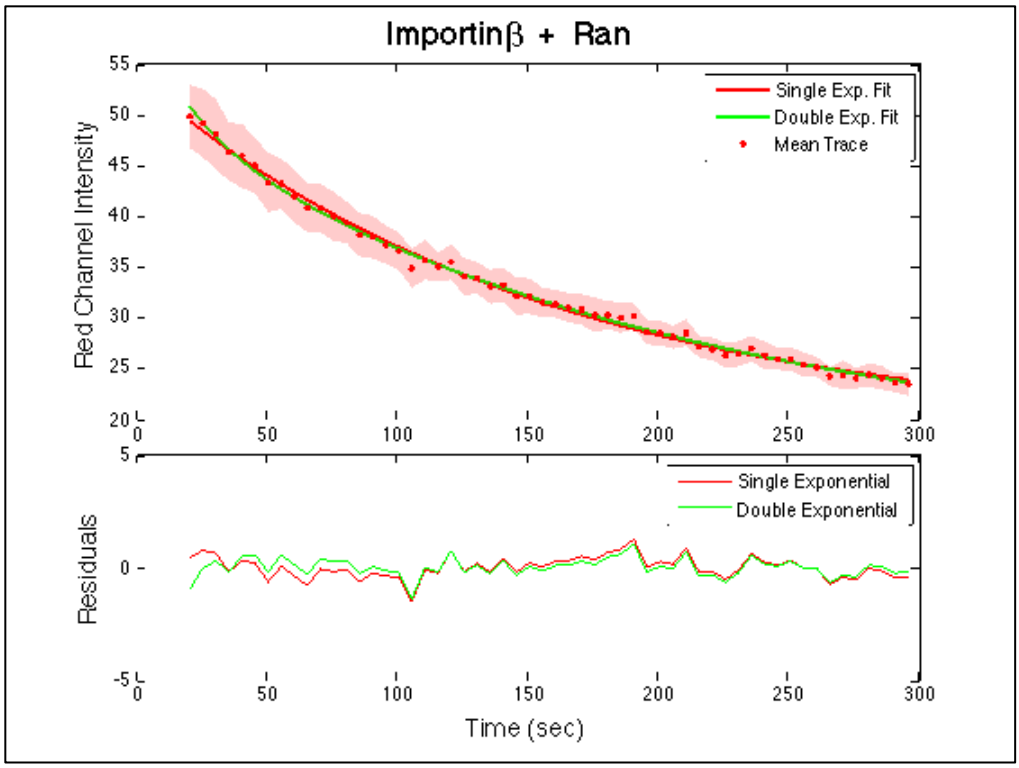

Figure 3.17 – Exponential Fit of Importin-β + Ran iFRAP Trace. The mean Importin-β +Ran iFRAP trace was fit with single and double exponential decay functions. The fits are shown in the top panel, and residuals are plotted in the bottom panel. The single-exponential fit does not generate any systematic error and is adequate to describe the system.

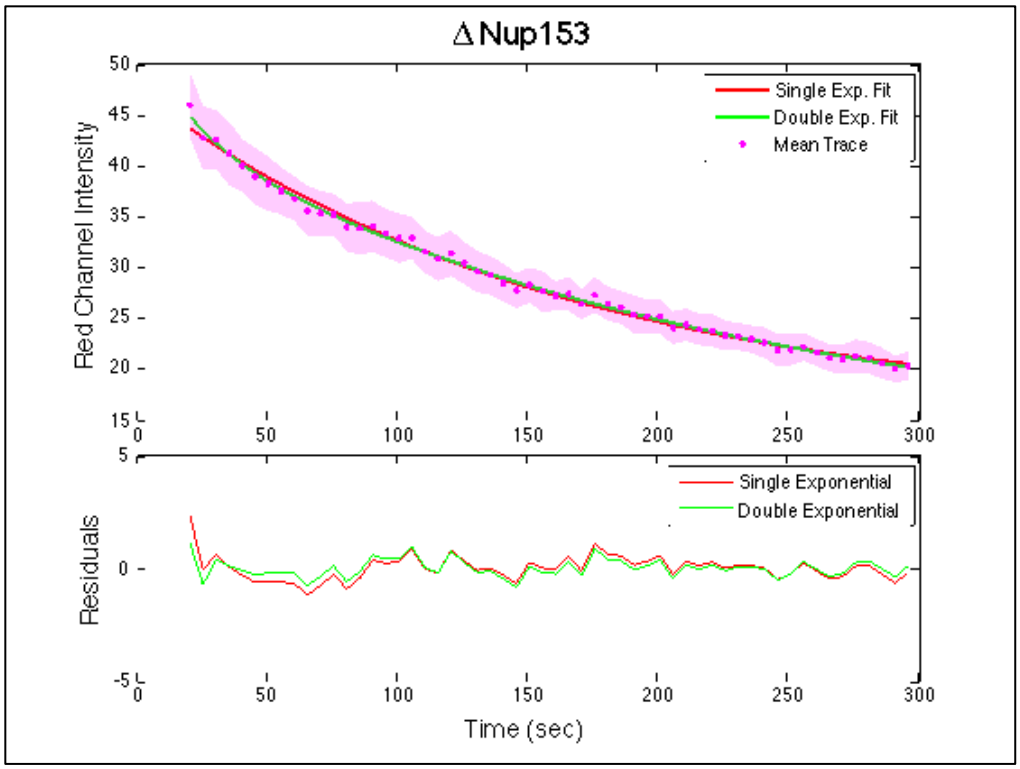

Figure 3.18 – Exponential Fit of ΔNup153 Cells + Importin-β iFRAP Trace. The mean ΔNup153 cells + Importin-β iFRAP trace was fit with single and double exponential decay functions. The fits are shown in the top panel, and residuals are plotted in the bottom panel. The single-exponential fit generates little to no systematic error and is adequate to describe the system.

	Curve Fitting							
	Single Exponential Decay			Double Exponential Decay				
	A	B	C	A	B	C	D	E
Importinβ	52	0.0082	26	30	0.055	50	0.0051	18
Importinβ + Ran	35	0.0065	19	10	0.049	35	0.0049	16
ΔNup153	32	0.0062	15	11	0.036	36	0.0031	6

Table 3.3 – Exponential Fit of iFRAP Data. This table displays the results of the exponential fits shown in figures 3.16-3.18.

3.4 - Materials and Methods

Protein expression and purification

Plasmid	Description	Resistance	Source
Importin-b	His_6 – Importin-b	Kanamycin	Steven Adam
Ran	His_6 – Ran	Kanamycin	Kalab *et al.*[1]
NTF2	His_6 – NTF2	Ampicillin	[Ref?]
YFP – Importin-b	His_6 – YFP – Importin-b	Kanamycin	This study
mEos2 – Importin-b	His_6 – mEos2 – Importin-b	Kanamycin	This study
2xGFP	His_6 – GFP – GFP	Kanamycin	This study

Plasmid construction: Plasmid constructs were synthesized using the SLIC procedure.[30] DNA primers were purchased from Elim Biopharmeuticals, Inc. XL1-Blue chemically competent *E. coli* cells were transformed and selected for by antibiotic resistance. Plasmids were purified using the Qiagen QIAprep Spin Miniprep Kit and sequenced.

Protein expression and purification: Proteins were expressed and purified as follows: *E. coli* (BL21 DE3) were transformed with the appropriate plasmid and a small number of colonies were picked from the plate into flasks containing 1 L of LB medium plus the appropriate antibiotic. The cells were grown at 37 °C to A600 of 0.6 and then induced with 0.5 mM IPTG overnight. Cells were harvested by centrifugation at 5000 g at 4 °C for 15 min and the pellet was resuspended in phosphate buffer (pH 7.4) containing 0.5 M NaCl, 20 mM imidazole, 1 mM β-mercaptoethanol and protease inhibitors (Roche Complete Protease Inhibitor Cocktail Tablet). Proteins were purified by Ni-NTA affinity chromatography. Proteins were typically dialysed into XB buffer (10 mM HEPES pH 7.7, 1 mM $MgCl_2$, 100 mM KCl, 50 mM sucrose), flash frozen in liquid nitrogen and stored at -80 °C. Protein purity was judged by SDS-PAGE, and concentrations determined by UV absorbance (using calculated extinction coefficients) or Bradford assays. Nucleotide loading of Ran was performed as follows: Briefly, the protein was incubated for 40 min on ice with 6 mM EDTA and a 50 fold excess of nucleotide (GDP or GTP). The reaction was stopped with a final concentration of 25 mM $MgCl_2$, added slowly. The protein was then dialysed against 30 mM potassium phosphate pH7.6, including 2 mM Mg-acetate, 2 mM GDP, 7% glycerol and 2 mM b-mercaptoethanol, at 4°C overnight.

Cell culture and permeabilization were performed as outlined in (Lowe *et al.*) The buffers used were:

- PBS (137 mM NaCl, 2.7 mM KCl, 8 mM Na2HPO4, 2 mM KH2PO4, pH 7.4)
- Permeabilization buffer (50 mM HEPES, 50 mM KOAc, 8 mM MgCl2, pH 7.3)
- Transport Buffer (20 mM HEPES, 110 mM KOAc, 5 mM NaOAc, 2mM MgOAc, 2 mM DTT, pH 7.3).

Hela cells were cultured in DMEM media (Gibco) and plated on glass bottomed (size 0 thickness) poly-lysine coated chambers (Mattek Corp.).

Cells were permeabilized according to the following protocol. The cells were washed for 3 x 2 min with PBS, followed by a 2 min wash with permeabilization buffer, followed by a 5 min permeabilization with digitonin (purchased from Sigma Aldrich) at a concentration of 50 ug/mL supplemented with an energy regenerating system of 100uM ATP, 100uM GTP, 4mM creatine phosphate, and 20u/mL creatine kinase) in permeabilisation buffer. The digitonin was subsequently removed by washing for 3 x 3 min with transport buffer. After the final wash, excess liquid was wicked off and the appropriate experimental reaction mix was quickly added to the cells. Control experiments with fluorescently (FITC) labelled dextrans (70 kDa) were used to confirm that the nuclear envelope remained intact following the digitonin permeabilisation.

rtFRAP assays: Digitonin-permeabilized HeLa cells were treated with a reaction mix containing a fluorescent transport receptor YFP-importin-ß (0.1uM WT Beta or mutant Beta), +/- RanGDP mixture, which included: RanGDP(5uM), NTF2 (4uM), and an energy regenerating system (2mM GTP, 0.1mM ATP, 4mM creatine phosphate, and 20u/mL creatine kinase) in transport buffer.
+/- RNAi knockdown of Nup153

iFRAP assays: Digitonin-permeabilized HeLa cells were treated with a reaction mix containing a fluorescent transport receptor mEos2 – Importin-b (0.1uM), +/- RanGDP mixture, which included: RanGDP(5uM), NTF2 (4uM), and an energy regenerating system (2mM GTP, 0.1mM ATP, 4mM creatine phosphate, and 20u/mL creatine kinase) in transport buffer.
+/- RNAi knockdown of Nup153

rtFRAP microscopy: Real-time FRAP was performed on a custom built microscope (Figure 2.19). The microscope allows one to perform simultaneous high-speed widefield imaging with a controlled diffraction limited bleaching/photoactivation spot at the center of the field of view. Briefly, four lasers (100 mW 405 nm Coherent Cube, and 100 mW 488, 514 and 561 nm Coherent Sapphires) were combined and expanded to a similar beam diameter. Each laser was under the controller of a shutter. Half-wave plates allow for adjustment of polarization. A Polarizing Beam Splitting cube (PBS) splits the beam into two “arms”. The ‘focused spot’ arm passes via a matched pair of convex lenses (f=50mm), one of which is mounted on a Z-translation stage to modify the focal depth position. An additional shutter in this arm allows for control of timing of the activation. The “imaging” arm has an additional lens (f=200mm) in order to focus the beam at the back focal plane of the objective (BFP). The two paths are recombined using a second PBS, and pass through a quarter wave plate before the remainder of the TIRF lens system to the objective (Olympus 60x 1.49N.A. TIRF apochromatic objective) via a multi-edge dichroic filter (Semrock). An actively cooled EMCCD camera (iXon+ or iXon Ultra)

was coupled to the camera port of the microscope via an additional magnifier. Sample positioning was controlled via a motorized stage with an additional XYZ-Nanopositioning stage (Physik Instrumente) for fine control. All software to control the microscope was written in C++.

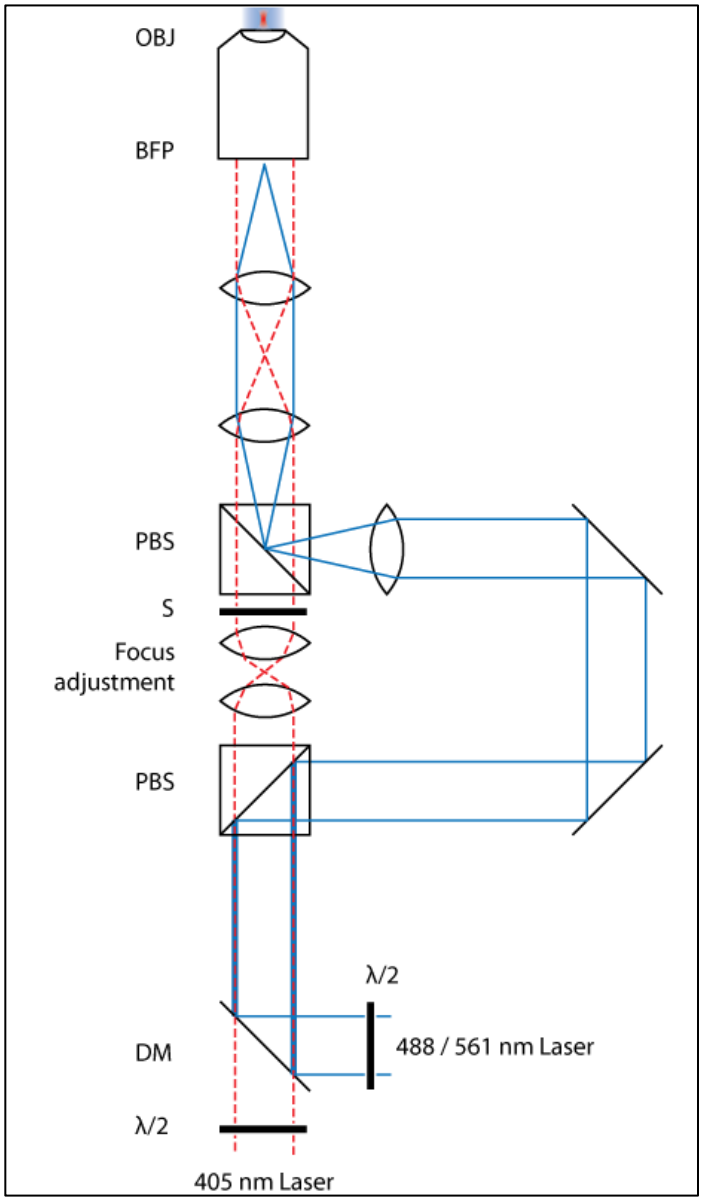

Figure 3.19 - Schematic of the optical set up of the Real-time Fluorescence Recovery After Photobleaching/Photactivation microscope (rtFRAP). Lasers are combined and passed through a Polarizing Beam Splitter (PBS) whereupon the polarized light is split into two paths. By adjusting the half-wave plates one can adjust the amount of light through either of the paths. A pair of lenses allows the adjustment of the diffraction limited spot focus along the optical axis. A shutter in this path controls temporal activation of the spot.

3.5 - References

[1] Peters, R., (2006). Introduction to nucleocytoplasmic transport: molecules and mechanisms. *Methods Mol. Biol.* 322, 235–258.

[2] Wente, S.R., Rout, M.P., (2010). The nuclear pore complex and nuclear transport. *Cold Spring Harb. Perspect. Biol.* 2, a000562.

[3] Pante, N, and M Kann. (2002). Nuclear pore complex is able to transport macromolecules with diameters of~ 39 nm. *Mol. Biol. Cell* 13(2), 425.

[4] Keminer, O., Peters, R. (1999). Permeability of single nuclear pores. *Biophys. J.* 77(1), 217-228.

[5] Ribbeck, K., Gorlich, D. (2001). Kinetic analysis of translocation through nuclear pore complexes. *EMBO J.* 20, 1320–1330.

[6] Siebrasse, J.P., Peters, R. (2002). Rapid translocation of NTF2 through the nuclear pore of isolated nuclei and nuclear envelopes. *EMBO Rep.* 3, 887–892.

[7] Cronshaw, J.M., Krutchinsky, A.N., Zhang, W., Chait, B.T., Matunis, M.J. (2002). Proteomic analysis of the mammalian nuclear pore complex. *J. Cell Biol.* 158, 915–927.

[8] Rout, M.P., Aitchison, J.D., Suprapto, A., Hjertaas, K., Zhao, Y., Chait, B.T. (2000). The yeast nuclear pore complex: composition, architecture, and transport mechanism. *J. Cell Biol.* 148, 635–651.

[9] Peters, R. (2009). Translocation through the nuclear pore: Kaps pave the way. *Bioessays* 31, 466–477.

[10] Denning, D.P., Patel, S.S., Uversky, V., Fink, A.L., Rexach, M. (2003). Disorder in the nuclear pore complex: the FG repeat regions of nucleoporins are natively unfolded. *Proc. Natl. Acad. Sci. U. S. A.* 100, 2450–2455.

[11] Pemberton, L.F., Paschal, B.M. (2005). Mechanisms of receptor-mediated nuclear import and nuclear export. *Traffic* 6, 187–198.

[12] Isgro, T.A., Schulten, K. (2005). Binding dynamics of isolated nucleoporin repeat regions to importin-beta. *Structure* 13, 1869–1879.

[13] Isgro, T.A., Schulten, K. (2007). Association of nuclear pore FG-repeat domains to NTF2 import and export complexes. *J. Mol. Biol.* 366, 330–345.

[14] Ben-Efraim, I., Gerace, L. (2001). Gradient of increasing affinity of importin beta for nucleoporins along the pathway of nuclear import. *J. Cell Biol.* 152, 411–417.

[15] Paradise, A., Levin, M.K., Korza, G., Carson, J.H. (2007). Significant proportions of nuclear transport proteins with reduced intracellular mobilities resolved by fluorescence correlation spectroscopy. *J. Mol. Biol.* 365, 50–65.

[16] Bayliss, R., Littlewood, T., Stewart, M. (2000). Structural basis for the interaction between FxFG nucleoporin repeats and importin-beta in nuclear trafficking. *Cell* 102, 99–108.

[17] Chi, N.C., Adam, S.A. (1997). Functional domains in nuclear import factor p97 for binding the nuclear localization sequence receptor and the nuclear pore. *Mol. Biol. Cell* 8, 945–956.

[18] Bischoff, F.R., Ponstingl, H. (1991). Catalysis of guanine nucleotide exchange on Ran by the mitotic regulator RCC1. *Nature* 354, 80–82.

[19] Mahajan, R., Delphin, C., Guan, T., Gerace, L., Melchior, F. (1997). A small ubiquitin-related polypeptide involved in targeting RanGAP1 to nuclear pore complex protein RanBP2. *Cell* 88, 97–107.

[20] Lee, S.J., Matsuura, Y., Liu, S.M., Stewart, M. (2005). Structural basis for nuclear import complex dissociation by RanGTP. *Nature* 435, 693–696.

[21] Lowe, A.R., Siegel, J.J., Kalab, P., Siu, M., Weis, K., Liphardt, J.T. (2010). Selectivity mech- anism of the nuclear pore complex characterized by single cargo tracking. *Nature* 467, 600–603.

[22] Zilman, Anton, Stefano Di Talia, Brian T Chait, Michael P Rout, and Marcelo O Magnasco. (2007). Efficiency, Selectivity, and Robustness of Nucleocytoplasmic Transport. *PLoS comp. biol.* 3(7), e125.

[23] J. Tang, unpublished results.

[24] J. Tang, unpublished results.

[25] Walther, T.C., Fornerod, M., Pickersgill, H., Goldberg, M., Allen, T.D. & Mattaj, I.W. (2001). The nucleoporin Nup153 is required for nuclear pore basket formation, nuclear pore complex anchoring and import of a subset of nuclear proteins*. EMBO J*. 20(20), 5703-14.

[26] Tokunaga, Makio, Naoko Imamoto, and Kumiko Sakata-Sogawa. (2008). Highly inclined thin illumination enables clear single-molecule imaging in cells. *Nat. Meth.* 5(2), 159-61.

[27] D. Görlich, N. Panté, U. Kutay, U. Aebi, F. R .Bischoff. (1996). Identification of different roles for RanGDP and RanGTP in nuclear protein import. *EMBO J.* 15(20), 5584–5594.

[28] U. Kutay, E. Izaurralde, F. R. Bischoff, I. W. Mattaj, D. Görlich. (1997). Dominant-negative mutants of importin-beta block multiple pathways of import and export through the nuclear pore complex. *EMBO J.* 16(6), 1153–1163.

[29] J. Tang, Unpublished Results.

[30] Li M.Z., Elledge S.J. (2007). Harnessing homologous recombination in vitro to generate recombinant DNA via SLIC. *Nat. Meth.* 4, 251–256.

Chapter 4
Spatial Distribution of Importin- β in the Nuclear Pore Complex

4.1 – Summary

Study of the dynamics of importin-β within the nuclear pore complex suggests that there are at least two classes of importin-β binding sites within the pore, high and low affinity classes. This chapter focuses on work to characterize the spatial distribution of importin-β molecules within the NPC, with the aim of identifying the regions of the pore where these sites are clustered. Super-resolution microscopy (dSTORM) was used to image dye-labeled importin-β within the NPC at a range of concentrations from 1nM to 0.5 μM.

4.2 – Introduction

The NPC is anchored in the nuclear envelope and has an octagonal spoke-ring structure surrounding a permeable channel, through which cargos are transported.[12] Flexible cytoplasmic filaments are attached to this core structure on the outer face of the pore, and the nuclear basket extends into the nucleoplasm.

The structure of the *Xenopus* NPC was characterized through cryo-electron microscopy, which showed that the pore is anchored within the nuclear envelope and has an internal transport channel with an axis that is normal to the envelope. These images also suggest that the internal channel has a bi-lobate, hourglass shaped structure with a tapered center. This channel is thought to be flexible and capable of undergoing conformational changes to accommodate import of large cargos.[3] A similar shaped nuclear pore structure was observed in cryo-EM studies of

the yeast NPC.[4] The flexible cytoplasmic filaments and nuclear basket associated with the core structure of the NPC have been imaged in the plant NPC.[5]

Importin-β Binding Affinity Gradient

The central channel of the NPC is lined with FG-Nups that bind importin-β and facilitate import. The binding affinities of importin-β for these FG-nups have been measured *in vitro*, showing a gradient of binding affinities that increases along the channel axis from the cytoplasmic to the nuclear face of the pore (Figure 4.1).

Binding affinity studies of importin-β have shown that the *in vitro* binding affinity of importin β for the nuclear basket FG-Nup, Nup153 (Kd = 9 nM) is approximately 10 fold greater than for Nup62 (Kd = 100–105 nM), which is found in the center of the pore transport axis, and approximately 200 fold greater than its affinity Nup358 (Kd = 210–225 nM), which is localized to the cytoplasmic face.[6]

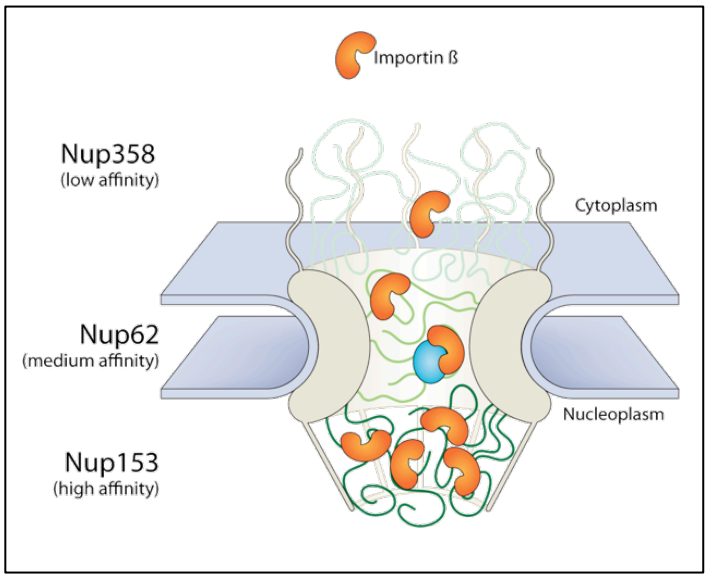

Figure 4.1 - Affinity gradient of FG-Nups within the NPC. This schematic diagram of the NPC shows the asymmetric distribution of FG-Nups within the pore, based on in vitro binding affinity measurements. An importin binding affinity gradient has been observed with increasing affinity along the import axis from the cytoplasmic face to the nuclear basket.

An equivalent affinity gradient for importin-β binding to FG-nups was observed in the yeast NPC (*S. cerevisiae*). The *in vitro* affinity of the Kap95 NTR-cargo complex for Nup1p—which is part of the nuclear basket, was found to be 225 fold greater than the complex affinity for Nup100p, which is located in the central scaffold of the pore, and 4000 fold greater than its affinity for Nup42p, which is localized to the cytoplasmic face of the NPC in yeast.[7]

High Affinity Binding Site: Necessary for Active Import

The presence of a high-affinity binding site at the nuclear face of the NPC appears to be necessary for efficient active nuclear transport. Deletion mutations to the highest affinity FG-Nup in the yeast NPC have been shown to decrease import efficiency.[8] Similar results have been observed for the human NPC; RNA interference knockdown of Nup153 shows reduced active transport in permeabilized HeLa cells.[9]

By characterizing the distribution importin-β within the NPC under a range of importin-β concentrations, the regions of high- and low-affinity binding sites can be located within the pore.

Super-resolution Microscopy

Light micrsocopy is widely used to study biological systems. However, the information that can be derived from these experiments is limited by the imaging resolution, which determines the minimal distance between to resolvable points in the field of view. In conventional microscopy, resolution limits result from the diffraction of light, which causes a point source signal to broaden as it travels toward the detector. The signal recorded by the detector can be approximated as a Gaussian distribution and is called the point spread function (PSF). The diffraction limit of light is determined by the full width half maximum of this Gaussian distribution and is approximately half the wavelength of light used to image the sample. Imaging of biological samples using fluorophores in the range of 450-650 nm emission yields a resolution limit of approximately 250nm.[10]

Super-resolution microscopy techniques, such as Photoactivated localization microscopy (PALM)[11] and stochastic optical reconstruction (STORM)[12] [13], can surpass the resolution limits imposed by the diffraction of light by using single-molecule localization methods.

In PALM and STORM low intensity activation light is directed at the sample, and individual molecules are stochastically activated. This causes them to emit light, which is detected as a diffuse, diffraction-limited spot or point spread function (PSF). The centroid of the PSF is localized with nanometer precision by fitting it to a Gaussian function, and hundreds of thousands to millions of such localized emissions are compiled into a single image. Correction for stage drift is typically performed using fluorescently labeled microscopic beads that are attached to the sample surface and serve as fiducials.

PALM is performed using photoactivatable fluorescent proteins that are expressed as a fusion protein to the protein of interest. STORM imaging can be performed using cyanine dye pairs that are chemically coupled to proteins of interest. Conventional fluorescent dyes, which can be induced to photoswitch under specific buffer conditions, can also be used.[14] [15] [16]

Super-resolution imaging provides high-resolution spatial distributions of labeled proteins[10], and has been used to image the eight-fold radial symmetry of the *Xenopus* NPC.[17] Single molecule imaging can provide insight into the distribution of importin-β in the pore with 10nm resolution.

4.3 - Results and Discussion

Super-resolution optical imaging was performed to determine the intrapore spatial distribution of importin-β. Permeabilized HeLa cells were treated with dye-labeled importin-β (at a range of concentrations from 1nM to 0.5 μM) and fixed with 4% paraformaldehyde. Importin-β was labeled with the AlexaFluor647 organic dye (Excitation/Emission 650nm/665nm). The cells were imaged on a custom built STORM microscope using a combination of 640nm and 488nm light. Low-intensity 488nm laser light was used to stochastically activate the organic dye molecules, and high-intensity 640nm light was used to image and deactivate the dye molecules. Drift correction was performed using dye-labeled beads that were adhered to the sample surface and imaged with 488nm light. The focal plane was set such that the image was a cross-section through the nucleus. This wide-field image shows a bright rim at the nuclear envelope and a fluorescent nucleoplasm (Figure 4.2).

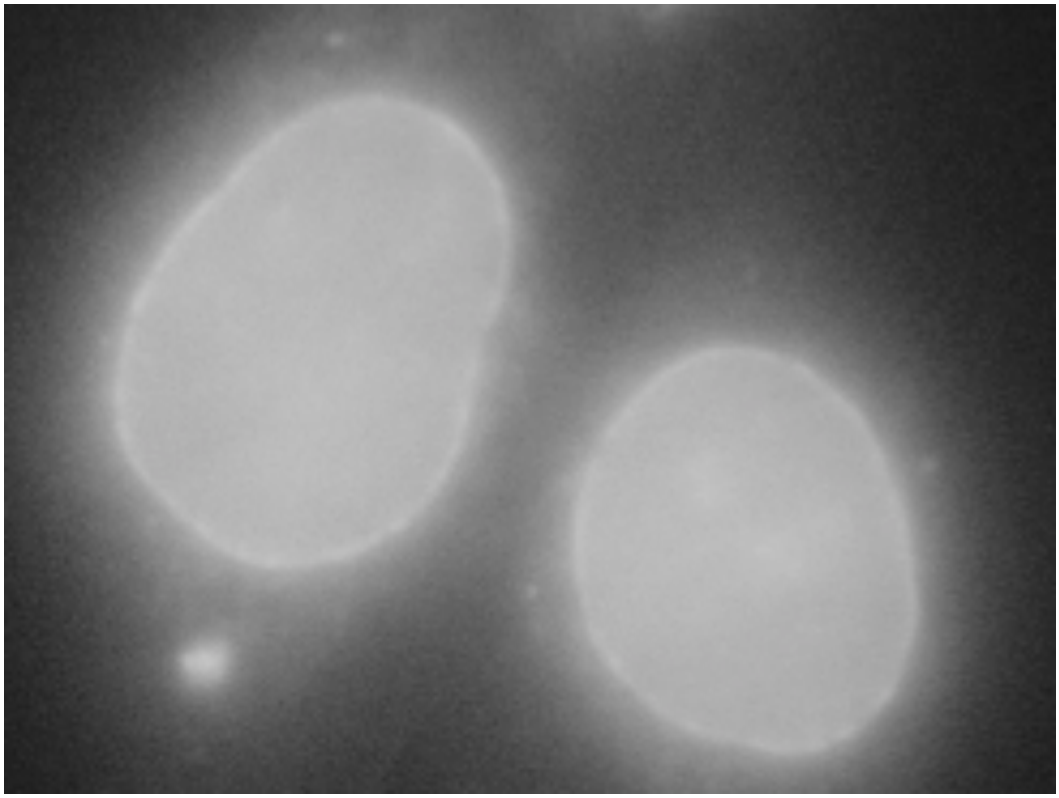

Figure 4.2 – Wide-field image of the dSTORM imaging focal plane. This wide-field image shows permeabilized HeLa cells that have been treated with dye-labeled importin-β (0.5uM). The image shows a bright rim at the nuclear envelope and a fluorescent nucleoplasm.

To reduce background fluorescence due to out of focus fluorophores, the principle of highly inclined and laminated optical sheet (HILO) microscopy was used.[18] The focal spot of the imaging laser on the back focal plane of the objective is translated such that the beam exits the objective at a low angle.

Dye-labeled importin-β molecules were localized with a mean spatial precision of ~10 nm (FWHM). Hundreds of thousands to millions of these localizations (depending on [importin-β]) were compiled into a STORM image. The image was refined by discarding out of focus localizations with point spread functions that did not conform to a Gaussian distribution with a defined standard deviation range. Discrete structures representing individual pores can be seen in the reconstructed images (Figure 4.3).

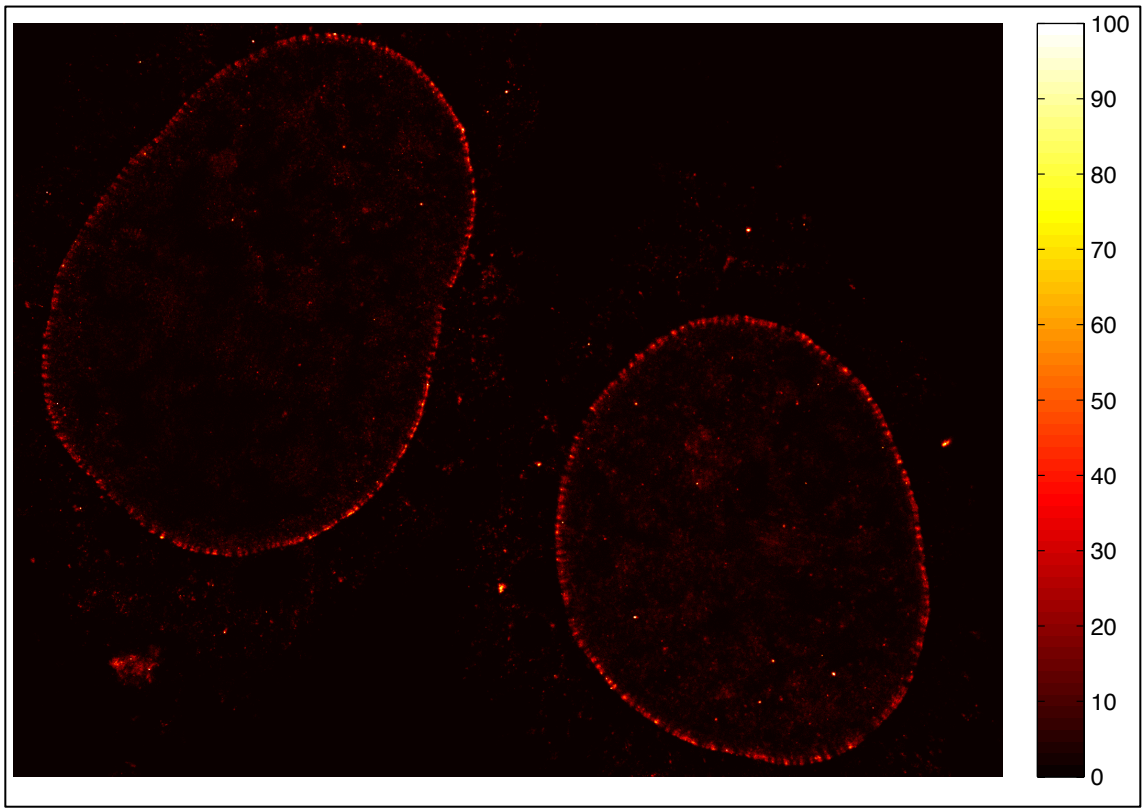

Figure 4.3 – dSTORM image of importin-β distribution in individual NPCs. This dSTORM image shows permeabilized HeLa cells that have been treated with dye-labeled importin-β (0.5uM). Individual pores can be seen in this image and appear as clusters of localizations along the nuclear envelope.

Computational methods were used to extract and align each NPC to generate an average map of importin-β distribution, and quantify the relative occupancy of importin-β in the pore under a range of concentrations (Figure 4.4).

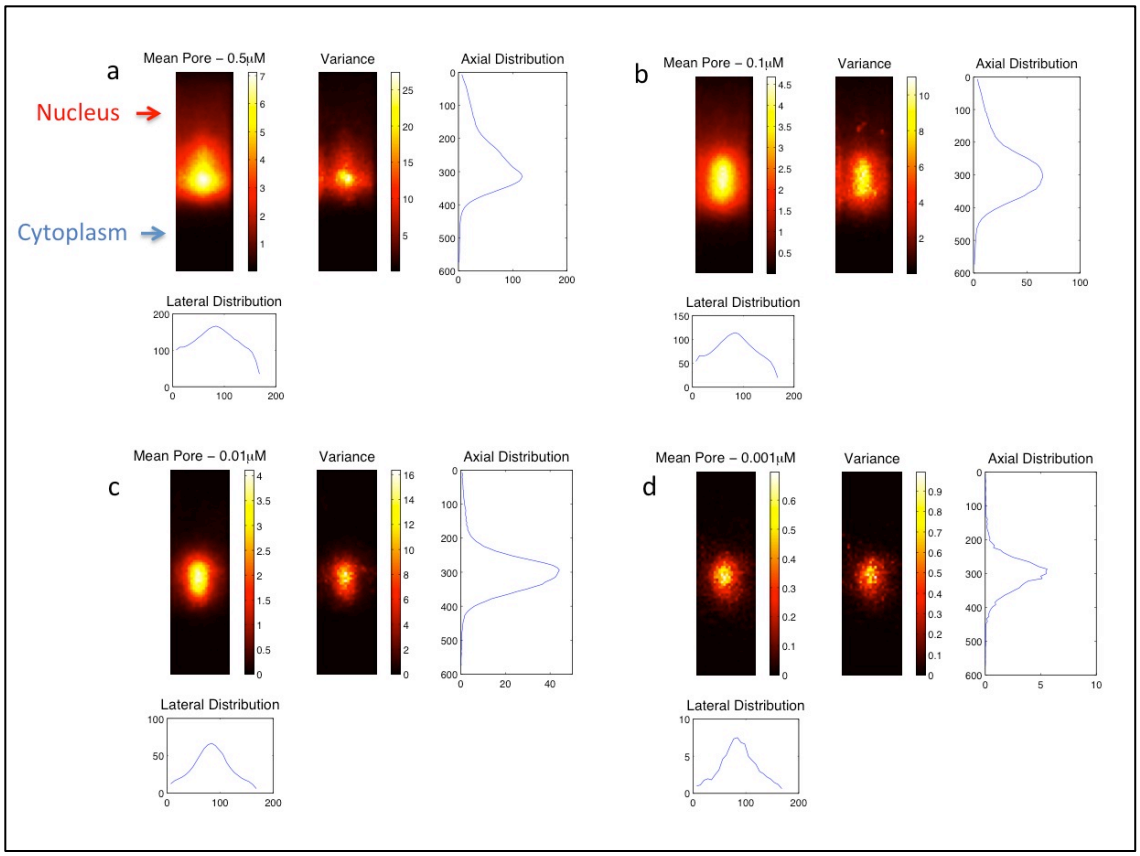

Figure 4.4 – Mean pore images, importin-β titration. dSTORM images of hundreds of individual NPCs were obtained for a range of importin-β concentrations: 0.5uM(a), 0.1uM(b), 0.01uM(c), 1nM(d), and 5nM. The individual pores were aligned, and mean pore images were generated. The axial and lateral distributions of importin-β are plotted.

An estimate for the pore dimensions based on these mean pore images is approximately 100-125nm by 50nm, agreeing well with previous studies.[16 19 20] Further characterization of pore dimensions would benefit from a two-color STORM image that provides a reference point in the NPC.

The NPC occupancy of importin-β increases with increasing concentration—ranging from 79 localizations at 1nM to 2299 localizations at 0.5μM importin-β (Figure 4.5b). Importin-β localizations were calculated by integrating the mean pore axial distribution curves between 200 and 400nm. The concentration dependence of pore occupancy is linear on a log-linear plot (Figure 4.5a). This indicates a saturating system and is consistent with the idea that there is a finite number of accessible binding sites for importin-β.

While these localizations cannot be used to directly count the number of importin-β molecules in the pore, they can be used to calculate the relative occupancy of importin-β under a range of concentrations. These measurements can be calibrated though importin-β counting experiments in individual NPCs.

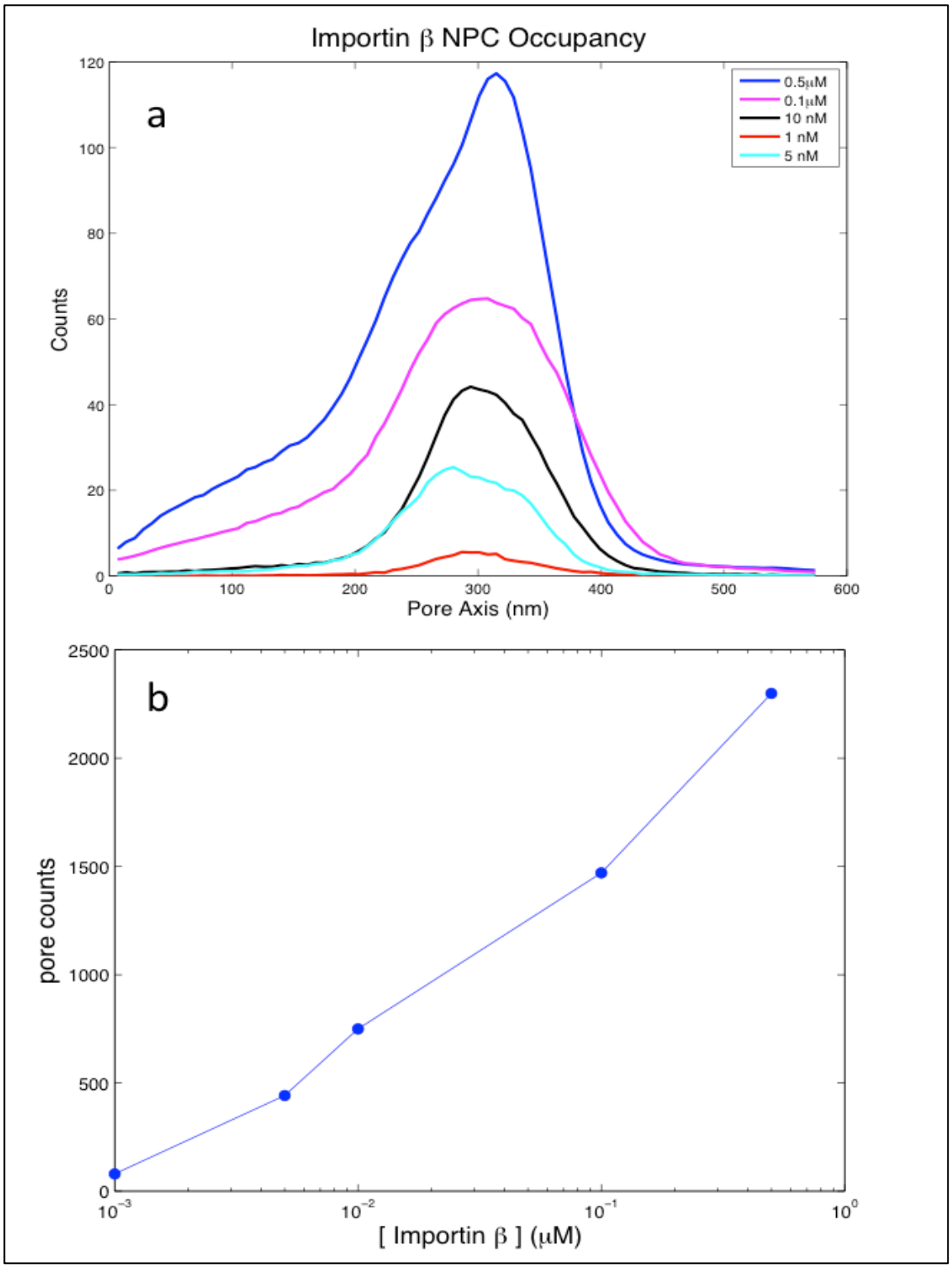

Figure 4.5 – Relative Occupancy of importin-β within the NPC. Axial distribution of importin-β is shown under a range of concentrations (a). Importin-β occupancy of individual NPCs increases with concentration. The concentration dependence of pore occupancy is linear on a log-linear plot (b). Relative occupancy is indicated by dSTORM localization counts.

Importin-β lateral distribution along the pore axis is altered upon titration of a range of importin-β concentrations. The shapes of the curves characterizing importin-β lateral distribution change with importin-β concentration. These curves suggest that the lateral distribution is biased toward the cytoplasmic face of the NPC at high concentrations of importin-β and shifted toward the nuclear face of the pore at low concentrations. This result is consistent with previous studies showing an affinity gradient of FG-Nups for importin-β, which increases along the pore axis toward the nucleoplasmic face.[21]

The main challenge in interpreting these results is the lack of a fixed reference point within the pore images that can be used to align the lateral distribution traces. A two-color STORM experiment could provide such a reference point.

4.4 - Materials and Methods

Cell preparation protocol
Cells were digitonin permeabilized as described in Chapter 2. Digitonin-permeabilized HeLa cells were treated with a reaction mix containing a fluorescently labeled transport factor YFP-importin-ß (various concentrations), +/- RanGDP mixture including: RanGDP(5uM), NTF2 (4uM), and an energy regenerating system (2mM GTP, 0.1mM ATP, 4mM creatine phosphate, and 20u/mL creatine kinase) in transport buffer. Import reactions proceeded at room temperature for 20 min before the cells were fixed with a 4% PFA solution for 15 min and washed 3 x 2 min with PBS. Fluorescent beads were then added to the cells and allowed to settle and affix to the surface for 15 minutes. Then the buffer was switched to STORM buffer and the cells were imaged.

STORM buffer
Imaging buffer: 100mM Mercaptoethylamine (Sigma Aldrich), Glucose Oxidase (Sigma Aldrich), Catalase (Sigma Aldrich), 10% (w/v) D-Glucose in PBS pH 7.4.

dSTORM imaging
All super-resolution imaging was performed on a custom built microscope, based on a Nikon TE-2000 base. Three lasers (100 mW 488 nm Coherent Sapphire, 100 mW 532 nm Coherent Compass and a 100 mW 640 nm Coherent Cube), each with their own shutter control, were expanded to the same diameter and combined using a series of dichroic mirrors into a single free-space beam. Half-wave plates were used to adjust the polarization before passing the beams through an Acousto-Optical Tunable Filter (AOTF, AA Optoelectronics, France) to modulate laser power. The combined beams were again expanded and passed through a quarter-wave plate to circularly polarize the beam. The free beam then passed through the TIRF lenses and was focused directly onto the back focal plane of the objective (Olympus 60x or 100x 1.49N.A. TIRF apochromatic objective) via a multi-edge dichroic filter (Semrock). An actively cooled EMCCD camera (iXon+ or iXon Ultra) was coupled to

the camera port of the microscope via an additional magnifier. Sample positioning was controlled via a micrometer stage with a XY-Nanopositioning stage (Mad City Labs). Focal drift during image acquisition was corrected using an Objective Z-Nanopositioning stage (Mad City Labs). Camera acquisition was at 40-120Hz. All software to control the microscope was written in C++ and Python. Data analysis was performed using custom software written in MATLAB, C++ and Python as outlined below.

Super-resolution Image Analysis

Sub-pixel localization of single-molecules: For a sub-wavelength diameter fluorescent molecule, fitting of the point spread function (PSF) to a Gaussian function yields the highest accuracy and precision of localization. Each PSF in successive dSTORM movie frames was fitted to a symmetrical 2D Gaussian function:

$$f(x,y) = Ae^{-\left(\frac{(x-x_0)^2}{2\sigma_x^2}+\frac{(y-y_0)^2}{2\sigma_y^2}\right)} + B$$

where A is the amplitude, B is the background, x_0 and y_0 are the mean x and y positions, and σ_x and σ_y are the standard deviations in x and y (where x=y for symmetrical Gaussian functions).

Drift correction was split into two parts: (i) Real-time focus locking performed during the imaging and (ii) post-imaging translational drift correction. We outline the two methods below:

(i) Real-time focus lock: Fluorescent beads (0.5µm Yellow-Green Fluospheres, Invitrogen) were immobilized to the glass surface of the chamber. The relative z-displacement of the equatorial imaging plane of the nucleus to the surface beads was measured. Imaging proceeded by alternating between imaging the surface beads and correcting for focus drift at the sample surface, and moving up to the imaging plane and performing dSTORM imaging. This was achieved using an automated script. Typically, focus drift was stabilized to within ~50 nm using this method.

(ii) XY stage translational drift correction: By tracking the fiducial markers at the sample surface plane over time, we can filter and interpolate their trajectories in order to correct the imaging plane movie sequences. We used the interpolated mean fiducial position in order to perform a per-frame drift correction. Typically, translational drift over the experiment was stabilized to within ~5 nm.

Localization precision

Localization precision was determined empirically. The localization precision of our instrument refers to how precisely we can define the centre of the PSF, given the

magnification and signal to noise ratio of the image. We experimentally determined the localization precision by immobilizing fluorescent dyes on to a glass coverslip and imaging them over time. The localisation precision is defined as the standard deviation of the positional distribution (σ_{xy}) of this particle. For each movie, we also determine the signal to noise ratio, a measurement of the quality of the image:

$$S/N = \frac{I_0 - I_b}{\sqrt{\sigma_0 \sigma_b}}$$

where I_0 and I_b are the intensities of the fluorophore and background signal respectively, and σ_0 and σ_b are the standard deviations in the intensity and background signals. Subsequently, the signal to noise ratio of each individual localisation was used to estimate its mean localization precision.

STORM images

Display images were created using the STORM localization data by bin-sorting the data with an appropriate bin size. Let K be the set of n STORM localizations $\{\mathbf{x}_1, \ldots, \mathbf{x}_n\}$. The data can be sorted into bins with size, h (typically 5-25 nm in size) according to the following equation:

$$\mathbf{I}_k = \left\lfloor \frac{1}{h} \mathbf{x}_k \right\rfloor, \text{ where } k \in K$$

and

$$\mathbf{x}_k = \begin{bmatrix} x_k \\ y_k \\ z_k \end{bmatrix}, \text{ where } z_k = 0 \text{ in 2D experiments.}$$

NPC identification, extraction and alignment: Individual NPCs were identified and extracted automatically. After identifying a closed path describing the nuclear envelope from widefield fluorescence and down-sampled dSTORM images, we use the interpolated surface normals of this path to position a sliding window normal to the envelope at positions along the envelope path. We count the localizations found within the window at each position along the envelope path. This envelope histogram contains distinct regions containing high numbers of localizations, which correspond to the centroids of NPCs (Figure 4.6).

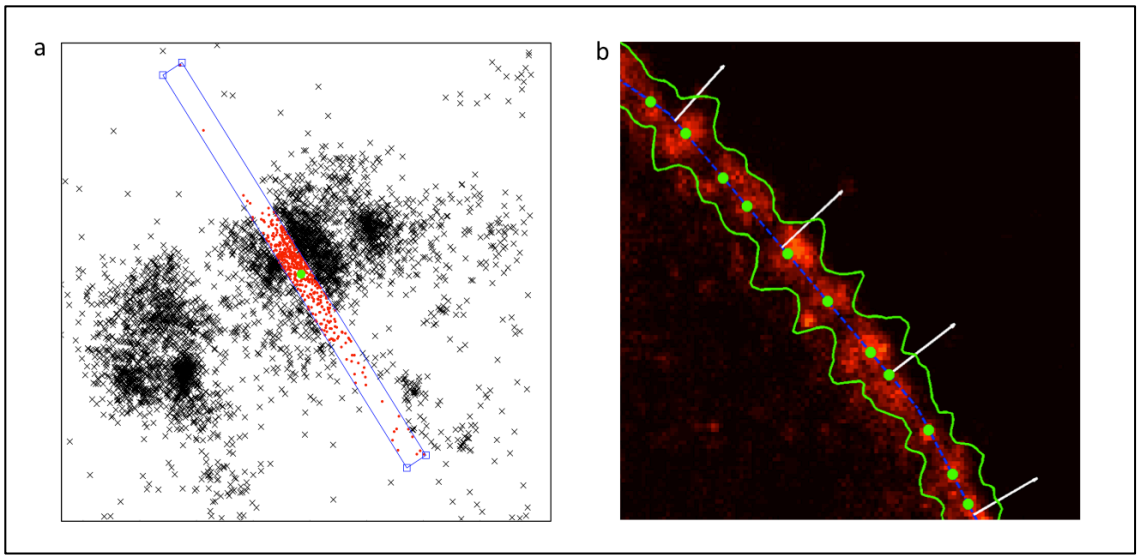

Figure 4.6 – STORM Image Analysis - After identifying a closed path describing the nuclear envelope, the interpolated surface normals of this path are used to position a sliding window normal to the envelope at positions along the envelope path (a). The localizations found within the window are counted at each position along the envelope path. This produces an envelope histogram, in which distinct regions containing high numbers of localizations correspond to the centroids of NPCs (b).

Having located the NPCs in the envelope, we use the interpolated surface normal to rotate the importin-b localizations corresponding to a single NPC into a common frame, whereby the cytoplasm-nucleus vector is oriented vertically down. Next we use a method of normalized cross correlation and reference-free alignment, to align each NPC image with sub-pixel resolution. Once all NPC structures are correctly aligned, we can calculate statistics including axial distributions, mean NPC images and positional variance maps.

4.5 - References

[1] Feldherr, C. M., Kallenbach, E. and Schultz, N. (1984). Movement of a karyophilic protein through the nuclear pore complex of oocytes. *J. Cell Biol.* 99, 2216-2222.

[2] Dworetzky, S. I. and Feldherr, C. M. (1988). Translocation of RNA-coated gold particles through the nuclear pores of oocytes. *J. Cell Biol.* 106, 575-584.

[3] Akey, C. W., and M. Radermacher. (1993). Architecture of the Xenopus nuclear pore complex revealed by three-dimensional cryo-electron microscopy. *J. Cell Biol.* 122(1), 1-19.

[4] Yang Q., Rout M.P., Akey C. (1998). Three-dimensional architecture of the isolated yeast nuclear pore complex: functional and evolutionary implications. *Mol. Cell* 1, 223–234.

[5] Fiserova, J., Kiseleva, E., and Goldberg, M.W. (2009). Nuclear envelope and nuclear pore complex structure and organization in tobacco BY-2 cells. *Plant J.* 59, 243–255.

[6] Ben-Efraim, I, and L Gerace. (2001). Gradient of increasing affinity of importin β for nucleoporins along the pathway of nuclear import. *J. Cell Biol.* 152(2), 411.

[7] Pyhtila, B., Rexach, M. (2003). A gradient of affinity for the karyopherin Kap95p along the yeast nuclear pore complex. *J. Biol. Chem.* 278, 42699–42709.

[8] Rexach, M.F. (2003). Disorder in the nuclear pore complex: the FG repeat regions of nucleoporins are natively unfolded. *Proc. Nat. Acad. Sci. USA* 100(5), 2450-5.

[9] J. Tang, Unpublished Results.

[10] Coltharp, C., Xiao, J. (2012). Superresolution Microscopy for Microbiology. *Cell. Microbiol.* 14(12), 1808–1818.

[11] Betzig, E., Patterson, G.H., Sougrat, R., Lindwasser, O.W., Olenych, S., Bonifacino, J.S., et al. (2006) Imaging intracellular fluorescent proteins at nanometer resolution. *Science* 313, 1642–1645.

[12] Rust, M.J., Bates, M., and Zhuang, X. (2006) Sub-diffraction- limit imaging by stochastic optical reconstruction micros- copy (STORM). *Nat. Meth.* 3, 793–795.

[13] Bates, M., Huang, B., Dempsey, G.T., and Zhuang, X. (2007). Multicolor super-resolution imaging with photo-switchable fluorescent probes. *Science* 317, 1749–1753.

[14] Folling, J., Bossi, M., Bock, H., Medda, R., Wurm, C.A., Hein, B., *et al.* (2008). Fluorescence nanoscopy by ground-state depletion and single-molecule return. *Nat. Meth.* 5, 943– 945.

[15] Heilemann, M., van de Linde, S., Schüttpelz, M., Kasper, R., Seefeldt, B., Mukherjee, A., *et al.* (2008). Subdiffraction- resolution fluorescence imaging with conventional fluorescent probes. *Angew. Chem. Int. Ed. Engl.* 47, 6172– 6176.

[16] Burnette, D.T., Sengupta, P., Dai, Y., Lippincott-Schwartz, J., and Kachar, B. (2011). Bleaching/blinking assisted localization microscopy for superresolution imaging using standard fluorescent molecules. *Proc. Natl. Acad. Sci. USA* 108, 21081–21086.

[17] Löschberger A., van de Linde S., Dabauvalle M.C., Rieger B., Heilemann M., Krohne G., Sauer M. (2012). Super-resolution imaging visualizes the eightfold symmetry of gp210 proteins around the nuclear pore complex and resolves the central channel with nanometer resolution. *J. Cell. Sci.* 125(3), 570-575.

[18] Tokunaga, Makio, Naoko Imamoto, and Kumiko Sakata-Sogawa. (2008). Highly inclined thin illumination enables clear single-molecule imaging in cells. *Nat. Meth.* 5(2), 159-61.

[19] Lowe, A.R., Siegel, J.J., Kalab, P., Siu, M., Weis, K., Liphardt, J.T. (2010). Selectivity mech- anism of the nuclear pore complex characterized by single cargo tracking. *Nature* 467, 600–603.

[20] Beck, Martin, Vladan Lucić, Friedrich Förster, Wolfgang Baumeister, and Ohad Medalia. (2007). Snapshots of nuclear pore complexes in action captured by cryo-electron tomography. *Nature* 449 (7162), 611-5.

[21] Ben-Efraim, I., and L. Gerace. (2001). Gradient of increasing affinity of importin β for nucleoporins along the pathway of nuclear import. *J. Cell. Biol.* 152(2), 411.

Chapter 5
Conclusion

NPC-mediated transport of materials between the cytoplasm and the nucleus is essential for many basic cell functions. This study set out to understand how the NPC facilitates directional transport across the nuclear envelope. The components of this molecular machine have been characterized, and there are several unproven models, which describe how these components might function in concert. However, many questions remain about how this system mediates selective transport of molecules while balancing this selectivity with speed.

Importin-β, Ran and Nup153 have been shown to be necessary for modulating selectivity of active and passive transport. Importin-β is required for active transport, and yet it blocks transport when present in excess.[1] Ran is also essential, and active import events do not take place in its absence.[2] Moreover, import efficiency is dramatically reduced in the absence of Nup153.

With regard to passive transport, importin-β mediates selectivity by blocking passive diffusion when present at high concentrations. Ran addition removes this blockage, speeding up transport and decreasing selectivity. RNAi knockdown of Nup153 also removes this passive import blockage.[3] Together these data suggest that Ran and Nup153 act in concert with importin-β to control pore function.

This study elucidates the mechanism by which importin-β interaction with the pore mediates selective, directional transport. Quantitative fluorescence microscopy, FRAP and super-resolution imaging are used to study the interplay of importin-β, Ran and Nup153 in regulating the selectivity and efficiency of the mammalian NPC.

FRAP and inverse FRAP (iFRAP) are utilized to measure the dynamics of importin-β turnover in the NPC, and super-resolution imaging is used to characterize its distribution in the pore. These data provide information about importin-β interactions with the FG-Nups in the pore, and about the mediation of these interactions by Ran and Nup-153.

FRAP and iFRAP experiments show that there are at least two phases of importin-β turnover in the pore—a slow phase on the timescale of minutes and a fast phase on the timescale of milliseconds to seconds. These phases correspond to at least two classes of importin-β populations, those bound to FG-Nups with high affinity and with low affinity respectively.

FRAP experiments also show that Ran adds a very fast turnover phase—on a millisecond timescale. Ran remodels the pore by actively turning over approximately 30% of the importin-β population. The turnover of this population is likely to be responsible for the Ran-induced increase in passive import in the experiments described above. This rapid turnover is also likely to be the necessary step for active transport, which cannot take place in the absence of Ran.

The site of Ran action on importin-β appears to be Nup153, as suggested by iFRAP results. In iFRAP experiments RNAi knockdown of Nup153 removes one phase in observed importin-β turnover, as compared to wild-type cells. Ran addition appears to have the same effect on the dynamics of importin-β —removing a turnover phase and yielding a similar iFRAP trace to the ΔNup153 case. This suggests that Ran preferentially acts on importin-β molecules that are bound to Nup153. This interpretation is consistent with preliminary STORM data characterizing the effects of Ran on importin-β distribution within the pore. These preliminary data show that Ran reduces the occupancy of importin-β at the nucleoplasmic face of the pore, where Nup153 is localized, but does not change the occupancy of the cytoplasmic face.[4] This hypothesis could be further tested by performing an iFRAP experiment with ΔNup153 knockdown cells in the presence of Ran. If this hypothesis is accurate, the curves should overlap.

The Ran-induced turnover of importin-β at Nup153 is consistent with the model postulating that Nup153 serves as a high-affinity trap for importin-β/cargo complexes, and that it is acted upon by a Ran-triggered release step.[5] This model is also consistent with previous work with functionalized Quantum Dot (QD) cargos, which showed that, in the absence of Ran (+GTP), these large QD cargos explore the entire NPC channel, but have a markedly reduced probability of exit into the nucleus.[2]

In addition to the Ran-induced fast turnover phase, a slowly turning over population of importin-β was also observed. FRAP and iFRAP data both show that a significant population remains within the pore over long timescales, greater than 15 minutes.

This result is somewhat surprising given the short timescale of active transport events, which take place within a fraction of a second.

Having observed this slow turnover phase, super-resolution microscopy was used to characterize the intrapore distribution of importin-β and to locate the region of high-affinity binding sites within the pore. STORM imaging of the NPC shows that importin-β distribution changes with concentration. The data suggest that importin-β distribution is biased toward the cytoplasmic face of the pore at high concentrations and shifted toward the nucleoplasmic face at low concentrations. This result is consistent with the kinetic data presented in this study, which point to the existence of at least two classes of importin-β binding sites within the pore—high and low affinity sites. It is also consistent with previous observations of an affinity gradient of FG-Nups for importin-β, which increases along the pore axis toward the nucleoplasmic face.[6] Collectively, these observations reinforce the notion of a high-affinity trap for importin-b/cargo complexes at the nucleoplasmic face of the NPC. Moreover, the use of STORM to characterize the effects of importin-β concentration on distribution demonstrates the use of super-resolution imaging to characterize the thermodynamics of this protein's interaction with the NPC.

This analysis could be strengthened with two-color STORM imaging that provides a reference point for alignment of pore images among different experimental conditions. Additionally, class averaging-based analysis of the data could be used to refine this analysis. Class averaging would make it possible to discern heterogeneous pore populations and detailed pore features, which are difficult to observe in mean pore images that average out variability.

The STORM data also show that occupancy of the NPC increases with importin-β concentration. The concentration dependence of pore occupancy is linear on a log-linear plot, suggesting that the pore is a saturating system with a finite number of binding sites accessible to importin-β. In the absence of Ran, the pore is saturated with importin-β at physiological concentration, a lower concentration than would be predicted by counting the number of FG-repeat binding sites. This suggests that that not all of these sites are simultaneously accessible to importin-β binding.

To calibrate these measurements of relative occupancy, a logical next step would be to quantify the number of importin-β molecules in the NPC through quantitative fluorescence photobleaching experiments of individual pores. STORM imaging provides relative measurements of pore occupancy, but due to repeated activation of fluorescent dye molecules, cannot be used to directly count the number of molecules present.

This study has shown that importin-β functions as an integral part of the NPC, as opposed to a soluble transport factor that only interacts transiently with the pore. Importin-β mediates selective, directional transport through dynamic interactions with FG-Nups in the pore. By dialing importin-β concentration up or down, the NPC

can increase and decrease active and passive import. This study has characterized the thermodynamics and kinetics of importin-β interaction with the pore and has shown how Ran and Nup153 mediate these interactions. Importin-β is an integral part of the NPC gate, and Ran acts to remodel this gate. The nucleoporin Nup153 plays a critical in the mechanism, acting as a coordinating site for importin-β and Ran action.

References

[1] J. Tang, Unpublished Results.

[2] Lowe, A.R., Siegel, J.J., Kalab, P., Siu, M., Weis, K., Liphardt, J.T. (2010). Selectivity mech- anism of the nuclear pore complex characterized by single cargo tracking. *Nature* 467, 600–603.

[3] J. Tang, Unpublished Results.

[4] A. Lowe and J. Tang, Unpublished Results.

[5] Zilman, A., S. Di Talia, B. T. Chait, M.P. Rout, and M.O. Magnasco. (2007). Efficiency, Selectivity, and Robustness of Nucleocytoplasmic Transport. *PLoS computational biology* 3(7), e125.

[6] Ben-Efraim, I., Gerace, L. (2001). Gradient of increasing affinity of importin beta for nucleoporins along the pathway of nuclear import. *J. Cell Biol.* 152, 411–417.

Appendix I
Long Timescale Inverse FRAP Experiments

To observe the turnover of importin-β in the nuclear pore complex (NPC) over long timescales, inverse FRAP (iFRAP) experiments were performed. These experiments were performed using similar methods as those described in Chapter 3. Permeabilized HeLa cells were treated with 0.1μM mEOS2 labeled importin-β. The photoswitchable fluourophore mEOS2 converts from a green to red fluorophore upon activation with 405nm laser light. A laser scanning confocal microscope was used to image the cells and photoactivate small segments of the nuclear envelope, and the nuclei were imaged in the green (488nm) and red (555nm) channels at 30-second intervals for 15 minutes. Images were analyzed using a MATLAB script that generates a mask for the nuclear envelopes, identifies the photoswitched cells in the field of view, and generates a mask for the photoswitched regions of the nuclear envelopes (Figure A1).

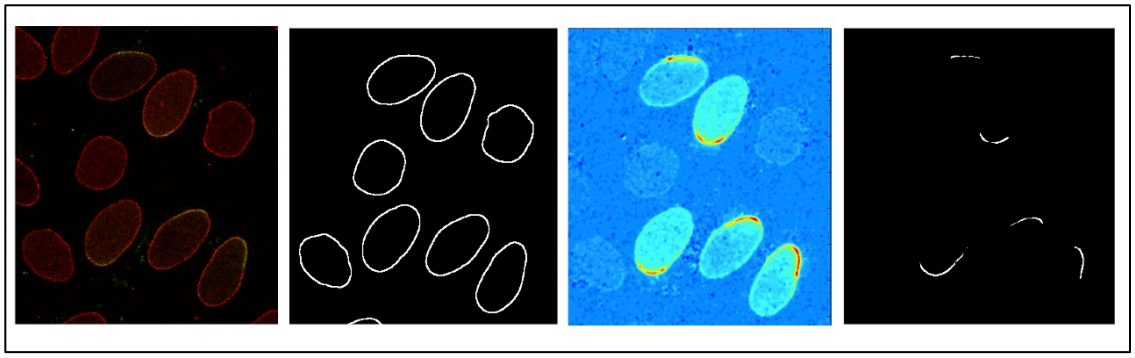

Figure A1 – Long timescale Inverse FRAP Experiment. The images show from left to right: a false-colored image of the nuclei with the photoswitched region indicated in green; the mask generated for the nuclear envelopes; a scaled image of the photoswithed regions of photoactivated cells; and a mask for the photoswitched regions of the nuclear envelopes.

These experiments generate raw iFRAP intensity traces for the photoswitched regions of the nuclear envelope and for the nuclear interior of all cells in the field of view (Figure A2).

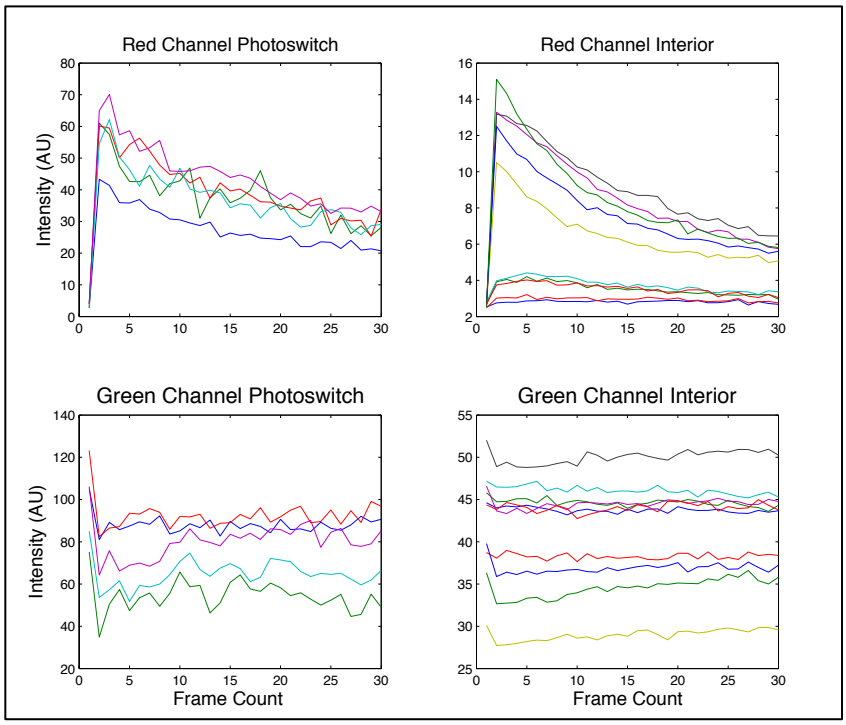

Figure A2 – Long Timescale iFRAP Raw Data. The iFRAP experiments generate raw intensity traces of the photoswitched regions of the nuclear envelopes in the red and green channels (left two panels). Intensity traces for the nuclear interior of all nuclei are also generated for both channels (right two panels). Frames correspond to 30-second time intervals.

The raw iFRAP data are then used to calculate mean traces for four experimental conditions: importin-β in wild type cells, importin-β + Ran in wild type cells, importin-β in wild type control cells, and importin-β in ΔNup153 cells (Figure A3). The wild type control cells were tested to control for the effects of the RNAi procedure. These cells received a similar treatment to the RNAi knockdown cells, but the RNA itself was not added.

The key result from these experiments is that, after 15 minutes, the fluorescence intensity decay traces do not return to zero. This suggests that there is a population of importin-β, which turns over very slowly and remains in the pore over long timescales. In addition, the experiments with wild-type control cells show that the RNAi procedure—absent RNA—generates similar results to untreated wild type cells and therefore does not generate experimental artifacts.

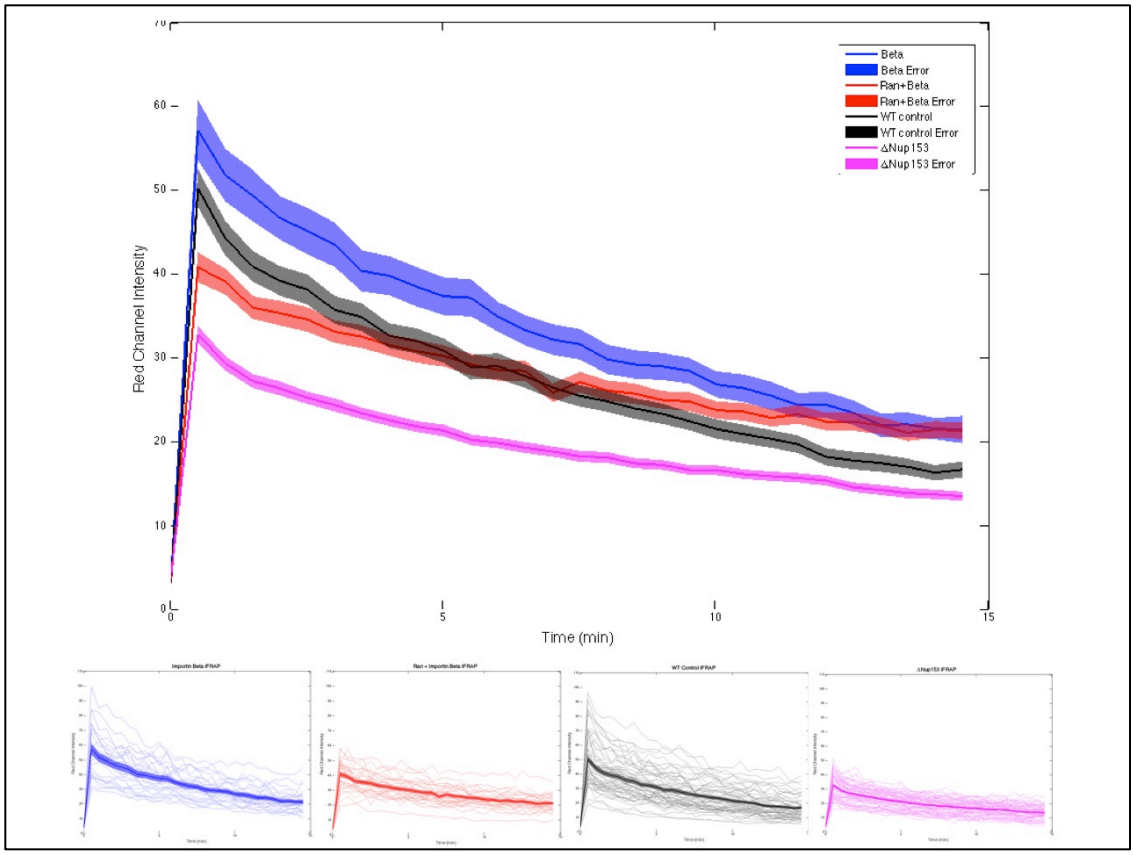

Figure A3 – Long Timescale Inverse FRAP Fluorescence Decay Traces. Mean iFRAP traces plotted with standard error of the mean are shown for four experimental conditions: importin-β in wild type cells (blue), importin-β + Ran in wild type cells (red), importin-β in wild type control cells (black) and importin-β in ΔNup153 cells (magenta). The raw data used to generate these mean traces are shown in the bottom panels.